

## Numerical investigation on VIV suppression of the cylinder with the bionic surface inspired by giant cactus

Wei Wang<sup>\*</sup>, Baowei Song, Zhaoyong Mao, Wenlong Tian, Tingying Zhang

School of Marine Science and Technology, Northwestern Polytechnical University, Xi'an, Shaanxi, China

### ARTICLE INFO

**Keywords:**

Vortex-induced vibration  
Numerical investigation  
Cylinder  
Bionic surface  
Giant cactus

### ABSTRACT

Vortex-induced vibration (VIV) responses of the cylinders with the bionic surfaces inspired by giant cactus are numerically studied, and the range of Reynolds number is  $8.0 \times 10^3 < Re < 5.6 \times 10^4$ . The dynamic response of the structure adopts Newmark-beta method. The effects of the height ratios ( $K_s/D$ ,  $K_s$  is the height of the bionic structure) on VIV suppression are discussed in detail, and five different height ratios ( $K_s/D$ ) include T1 ( $K_s/D = 0.000$ ), T2 ( $K_s/D = 0.025$ ), T3 ( $K_s/D = 0.050$ ), T4 ( $K_s/D = 0.075$ ) and T5 ( $K_s/D = 0.100$ ). The VIV response process is characterized by four sub-regions (Region I, Region II, Region III and Region IV). As the height ratios of the bionic structures increase, the range of the large-amplitude-motion region gradually decreases, and the lock-in range is smaller. The maximum amplitude ratio in cross-flow direction decreases from 1.50 (T1) to 0.75 (T5), and it reduces by about 50%. The maximum in-line amplitude ratio decreases from 0.35 (T1) to 0.12 (T5), which reduces by about 65.7%. For T1 and T2, the jump phenomenon of frequency ratio occurs between region II and region III. However, the jump phenomenon of frequency ratio occurs between region I and region II for T3, T4 and T5. The maximum mean-drag-coefficient decreases from 3.00 (T1) to 2.25 (T5), and it reduces by about 25%.

### 1. Introduction

Vortex-induced vibration (VIV) is a typical Fluid-Structure Interaction (FSI) phenomenon. VIV often occurs in the fields of nuclear engineering, wind engineering, renewable energy engineering and ocean engineering (Ding et al., 2015; Wang et al., 2019a; Xu et al., 2019). Because VIV is related to the structural design in many practical projects, VIV has attracted more and more concern. When the vortex shedding frequency approaches to the natural frequency of the structure, a large-amplitude motion is observed, called “lock-in” or vortex synchronization (Dorogi and Baranyi, 2018). Especially, “lock-in” causes more serious consequence for a low mass-damping system, which is one of the important factors in fatigue failure and structure instability (Franzini et al., 2018; Wang et al., 2020).

There are many numerical and experimental investigations on VIV suppression. VIV suppression methods are divided into two categories based on the presence or absence of energy input (Rashidi et al., 2016; Zdravkovich, 1981). If energy input is required, the suppression method is an active method. On the contrary, the suppression method is a passive method. Some typical examples of active methods are electrical methods (Artana et al., 2003), feedback control methods (Carini et al.,

2014), rotary oscillation (Lee and Lee, 2008), suction and blowing (Muralidharan et al., 2013), thermal effect (Chatterjee D., 2014) and synthetic jets (Wang et al., 2019(b)). Obviously, the active methods are more complex and costly. However, the passive methods are simpler and are used in practical engineering. The following mainly introduces some typical examples of passive control. Zhu and Yao (2015) have done a lot of researches on the control rods using numerical methods, and the effects of Reynolds number, diameter ratio ( $d/D$ ), control rod number ( $N$ ) and spacing ratio ( $G/D$ ) on VIV suppression were investigated. The results showed that placing some control rods at the appropriate positions could suppress VIV response well, and the optimal parameters were  $d/D = 0.15$ ,  $N = 9$  and  $G/D = 0.6$ . Law and Jaiman (2017) studied the low-drag wake stabilization devices on VIV suppression using numerical methods, and four new wake devices were presented. The results showed that C-shaped device not only reduced the drag force of the system, but also prevented the occurrence of galloping in the high Reynolds number range. Wang et al. (2018) presented a flexible plate installed on the cylinder, and the results showed that VIV responses were controlled. Sui et al. (2016) experimentally studied the cylinder attached with helical strakes on VIV suppression, and the maximum suppression efficiency reached up to 98%. Huera-Huarte (2017) investigated the wire meshes on VIV suppression, and the maximum

\* Corresponding author.

E-mail address: [wangwei0908@mail.nwpu.edu.cn](mailto:wangwei0908@mail.nwpu.edu.cn) (W. Wang).

### Nomenclature

$D$	Diameter of the cylinder	$v$	Kinematic viscosity of water
$K$	Spring stiffness	$D_s$	The actual diameter of the cylinder
$f_s$	Vortex shedding frequency	$C$	Damping
$F_x, F_y$	Fluid forces	$f_n$	Natural frequency of the cylinder
$m_a$	Added-mass of the system	$m$	Mass of the system
$M$	Total mass of the system	$C_A$	Added-mass coefficient
$U$	Flow velocity	$m^*$	Mass-ratio
$Re$	Reynolds number	$U_r$	Reduced velocity
$C_L$	The lift coefficient	$N$	The number of ribs
$D_s$	The actual diameter of the cylinder	$C_d$	The drag coefficient
$A_x, A_y$	Displacements	$K_s$	The height of the bionic surface
		$\rho$	Water density
		$L$	The length of the cylinder ( $L = 1$ m)

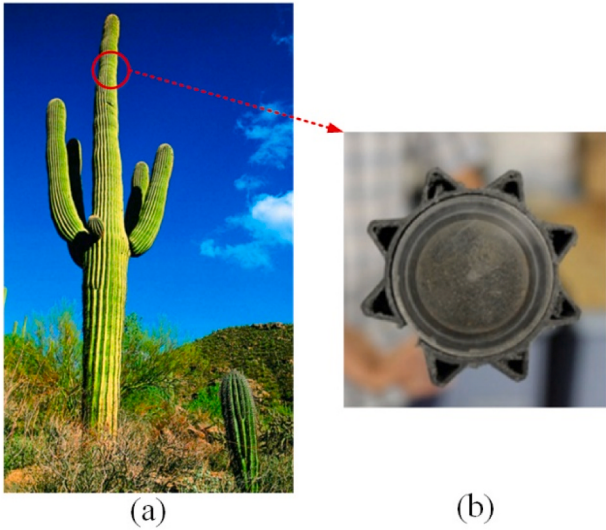


Fig. 1. (a) The giant cactus in the desert; (b) the cross-section of the giant cactus.

suppression efficiency of amplitude responses was more than 95% and the drag coefficient could be reduced by up to 20%. Zhu et al. (2017) presented a free-to-rotate triangular fairing on VIV suppression, and results showed that the characteristic length and the rotational friction have great influence on VIV suppression.

In addition to the above passive control methods by installing additional devices, VIV suppression can also be achieved by directly changing the surface of the structure. Gao et al. (2018) studied the different surface roughness of the cylinder, and four different roughness

values ( $K_s/D = 0, 0.005, 0.010$  and  $0.020$ ) were presented. The results showed that the cross-flow amplitude decreased with the increase of the surface roughness, and the VIV response region was only divided into two branches. The surface roughness on VIV suppression were also studied experimentally by Kiu et al. (2011). Law and Jaiman (2018) investigated the spanwise grooves on VIV suppression, and the cross-flow amplitude was suppressed up to 37% and the drag coefficient was reduced by about 25%. Huang (2011) presented a triple-starting helical groove on VIV suppression, and the depth of the groove is  $0.16D$  and the width is  $0.2D$ . The results showed that the cross-flow vibration amplitude was reduced by about 64%. The structural features of giant cactus in the desert are critical to their survival, and giant cactus in the desert are as show in Fig. 1. Some ribs and spines can not only play an important role in control of water evaporation from the plants, but also help to decrease wind loads and to prevent wind damage and uprooting by changing the flow around the plant. The drag coefficient and the fluctuating lift coefficient could be effectively reduced. The classical ribbed cylinder has 24 V-shaped grooves (Yamagishi and Oki, 2005). There are some investigations on the aerodynamic characteristics of the cactus-inspired cylinders. However, whether a circular cylinder with bionic surface inspired by giant cactus have better hydrodynamic characteristics? Whether VIV responses of the cylinder with the bionic surface can be suppressed? Furthermore, whether the height characteristics of the bionic surfaces can affect VIV responses? Therefore, a circular cylinder with the bionic surface inspired by giant cactus are investigated on VIV suppression, and the height ratios of the bionic surface are investigated in detail.

In this study, VIV responses of the cylinders with the bionic surfaces of different height ratios are numerically studied. The numerical simulation is resolved using computational fluid dynamics (CFD) methods. The problem description is shown in Section 2, and the computational method is shown in Section 3. The effects of the bionic surfaces with different height ratios on VIV suppression are discussed in Section 4.

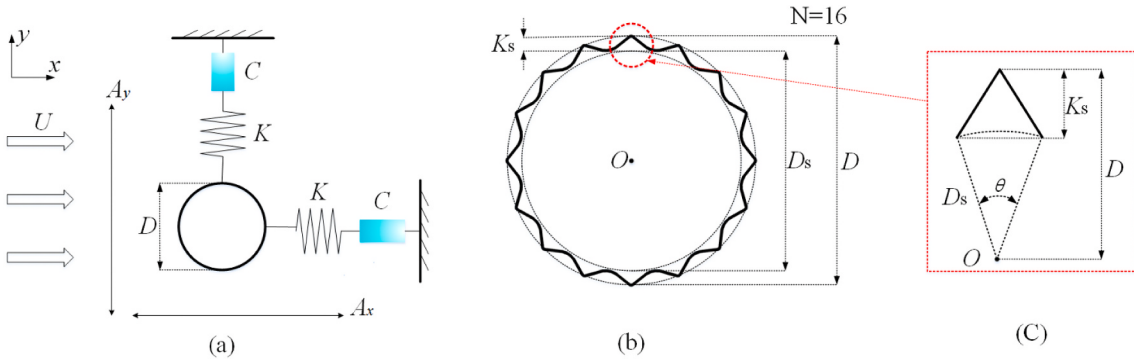
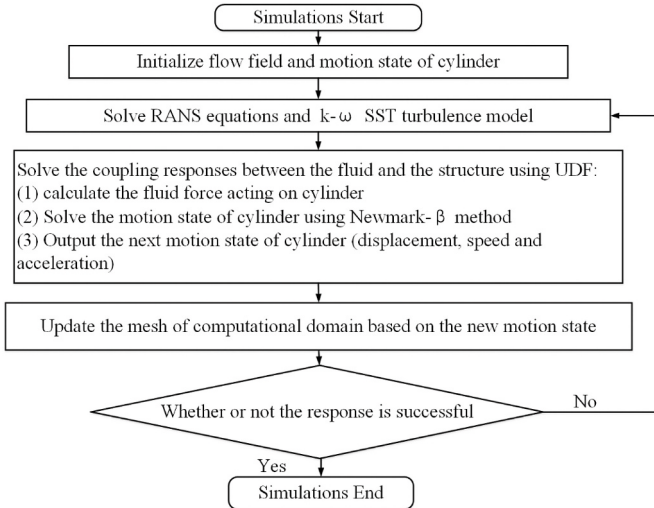


Fig. 2. (a) VIV system; (b) the cylinder with the bionic surface; (c) the bionic structure.

**Table 1**  
The VIV system parameters.

Denomination	Symbol	Value
Spring stiffness	$K$ (N/m)	178.6
Damping-ratio	$\xi$	0.005
Natural frequency in water	$f_n$ (Hz)	0.4
Mass-ratio	$m^*$	2.6
Water density	$\rho$ (kg/m <sup>3</sup> )	1000
Kinematic viscosity	$\nu$ (m <sup>2</sup> /s)	$1.0 \times 10^{-6}$
Diameter of circular cylinder	$D$ (m)	0.1



**Fig. 3.** The process of numerical calculation.

Section 5 shows some important conclusions.

## 2. Problem description

### 2.1. Investigated geometries

A cylinder, two dampers and two springs are included in the two-degree-of-freedom (2-DOF) VIV system, as shown in Fig. 2(a). Fig. 2(b) is a schematic diagram of a cylinder with the bionic surface. Fig. 2(c) is the geometry of the bionic structure.  $K$  is the spring stiffness and  $C$  is

the system damping. The height of the bionic surface is  $K_s$ . The bionic surface is composed of many ribs and the number of ribs is usually 10–30 (Yamagishi and Oki, 2005). The number of ribs ( $N$ ) is 16 in this study. The shape of the bionic structure is triangle as shown in Fig. 2(c), and the angle of the arc corresponding to the bottom edge of the bionic structure is  $\theta$ . When  $N = 16$ ,  $\theta/2\pi = 0.05$  (Yamagishi and Oki, 2005).  $D$  is the outer diameter of the cylinder, which keeps the same for all cases.  $D_s$  is the inner diameter of the cylinder. In most previous studies, the inner diameter ( $D_s$ ) was a more general choice for the definition of bare cylinder and usually kept the same. However, there were also some studies about grooves on the surface of the cylinder. When the effect of grooves on the flow around the cylinder was studied, the outer diameter ( $D$ ) was usually selected. Because the area in in-line direction will not change when  $K_s$  and  $D_s$  change if the outer diameter ( $D$ ) is selected, this selection method is helpful to compare the changes in the drag force and drag coefficient (Law and Jaiman, 2018). The five different height ratios ( $K_s/D$ ) of the bionic surface are investigated, including 0, 0.025, 0.050, 0.075 and 0.100. Table 1 shows the parameters of 2-DOF system. The vibration in in-line direction and the vibration in the cross-flow direction is all considered in 2-DOF VIV system.

### 2.2. Motion equations

In order to resolve the 2-DOF VIV response, the mass-spring-damper model is established. The equations of system can be expressed as (Wang et al., 2019(c)):

$$m \cdot \ddot{x} + C \cdot \dot{x} + K \cdot x = F_x(t) \quad (1)$$

$$m \cdot \ddot{y} + C \cdot \dot{y} + K \cdot y = F_y(t) \quad (2)$$

where

**Table 2**  
The validation of mesh dependence.

Mesh	Elements	$A_y/D$	$f_s/f_n$
Q1	$3.0 \times 10^4$	0.8600	1.2238
Q2	$6.0 \times 10^4$	0.8686 (10.00%)	1.2418 (1.47%)
Q3	$9.0 \times 10^4$	0.8742 (0.64%)	1.2488 (0.56%)
Q4	$1.2 \times 10^5$	0.8765 (0.26%)	1.2508 (0.16%)
Q5	$1.5 \times 10^5$	0.8769 (0.05%)	1.2513 (0.04%)

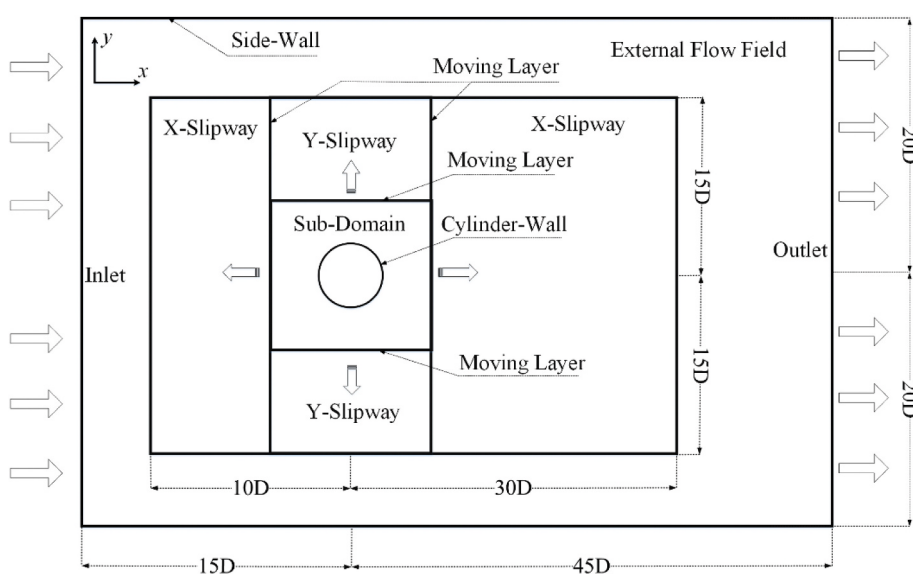


**Fig. 4.** The computational domain.

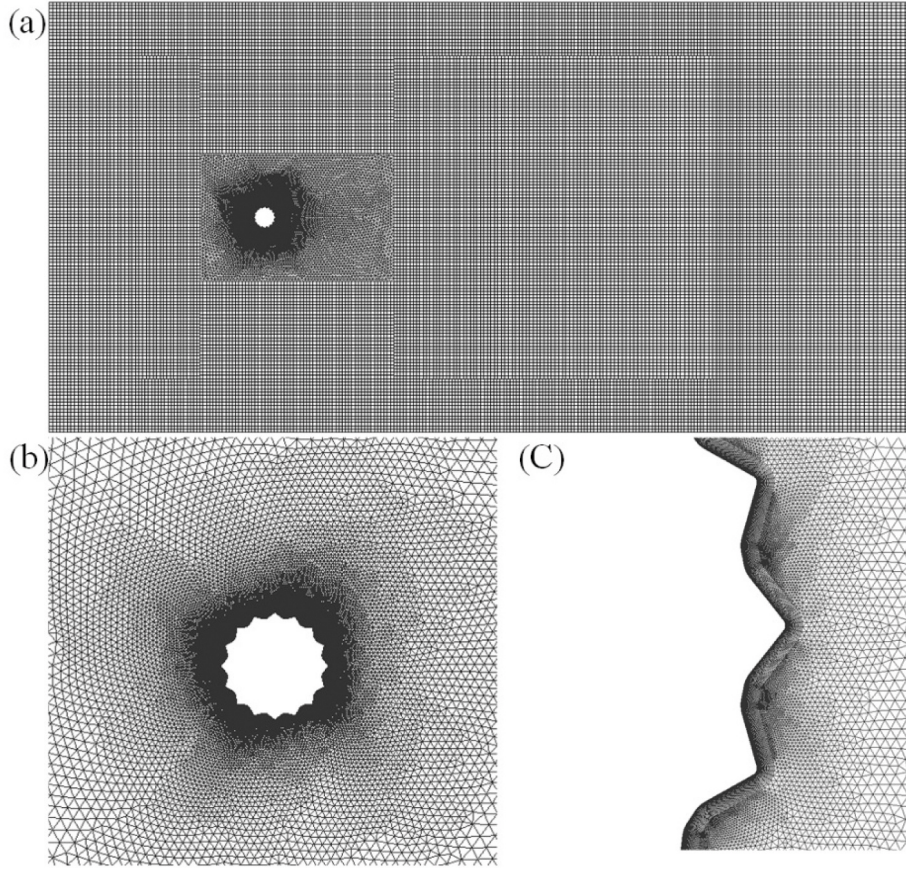


**Fig. 5.** Mesh:(a) the computational domain; (b) the cylinder; (c)the boundary-layer.

$$m = m^* \cdot \frac{D^2}{4} \cdot \pi \cdot \rho \cdot L \quad (3)$$

$$M = m + m_{add} \quad (4)$$

$$m_{add} = C_A \cdot \frac{D^2}{4} \cdot \pi \cdot \rho \cdot L \quad (5)$$

$$C = 2 \cdot \sqrt{K \cdot M} \cdot \xi \quad (6)$$

$$f_n = 2\pi \cdot \sqrt{\frac{K}{M}} \quad (7)$$

in which,  $x$ ,  $\dot{x}$  and  $\ddot{x}$  are the displacement, velocity and acceleration in  $x$ -direction and  $y$ ,  $\dot{y}$  and  $\ddot{y}$  represent the same quantities in  $y$ -direction.  $C_A$  is the added mass coefficient ( $C_A = 1$  for the cylinder (Zhu et al., 2017)).

### 3. Computational method

#### 3.1. Mathematical model

The two-dimensional unsteady RANS equations in conjunction with SST/k- $\omega$  turbulence model are used in numerical simulation (Wang et al., 2019(b)). User-Defined Functions (UDF) are embedded in Fluent for resolving the VIV response.

The vibration responses of the structure are resolved by using the

Newmark- $\beta$  method in UDF (Pasetto et al., 2019). In order to solve velocity and displacement, two parameters ( $\alpha$  and  $\beta$ ) are introduced.

The two basic equations are expresses as follows:

$$u_{t+\Delta t} = u_t + \dot{u}_t \cdot \Delta t + [(1/2 - \beta) \cdot \ddot{u}_t + \beta \cdot \ddot{u}_{t+\Delta t}] \cdot \Delta t^2 \quad (8)$$

$$\dot{u}_{t+\Delta t} = \dot{u}_t + [(1 - \alpha) \cdot \ddot{u}_t + \alpha \cdot \ddot{u}_{t+\Delta t}] \cdot \Delta t \quad (9)$$

Considering Eq. (8) and Eq. (9),  $\ddot{u}_{t+\Delta t}$  and  $\dot{u}_{t+\Delta t}$  can be expressed as:

$$\ddot{u}_{t+\Delta t} = \frac{1}{\beta \cdot \Delta t^2} (u_{t+\Delta t} - u_t) - \frac{1}{\beta \cdot \Delta t} \dot{u}_t - \left( \frac{1}{2\beta} - 1 \right) \cdot \ddot{u}_t \quad (10)$$

$$\dot{u}_{t+\Delta t} = \frac{\alpha}{\beta \cdot \Delta t} (u_{t+\Delta t} - u_t) + \left( 1 - \frac{\alpha}{\beta} \right) \cdot \dot{u}_t - \left( \frac{\alpha}{2\beta} - 1 \right) \cdot \Delta t \cdot \ddot{u}_t \quad (11)$$

Unknown items  $u$  can represent  $x$  or  $y$ . Based on Eq. (8) and Eq. (9), Eqs. (1) and (2) can be unified as:

$$m \cdot \ddot{u}_{t+\Delta t} + C \cdot \dot{u}_{t+\Delta t} + K \cdot u_{t+\Delta t} = F_{fluid}(t)_{t+\Delta t} \quad (12)$$

$\alpha$  and  $\beta$  are 0.5 and 0.25 (Wang et al., 2019(b)). Based on Eqs. (10)–(12), items  $\ddot{u}_{t+\Delta t}$ ,  $\dot{u}_{t+\Delta t}$  and  $u_{t+\Delta t}$  can be solved.

Finally, Eq. (12) can be expressed as:

$$[\bar{K}] \cdot u_{t+\Delta t} = [\bar{F}] \quad (13)$$

$$\text{where } [\bar{K}] = K + \frac{1}{\beta \cdot \Delta t^2} M + \frac{\alpha}{\beta \cdot \Delta t} C,$$

$$[\bar{F}] = F_{fluid}(t)_{t+\Delta t} + \left[ \frac{1}{\beta \cdot \Delta t^2} \cdot u_t + \frac{1}{\beta \cdot \Delta t} \cdot \dot{u}_t + \left( \frac{1}{2\beta} - 1 \right) \cdot \ddot{u}_t \right] \cdot M + \left[ \frac{\alpha}{\beta \cdot \Delta t} \cdot u_t + \left( \frac{\alpha}{\beta} - 1 \right) \cdot \dot{u}_t + \left( \frac{\alpha}{2\beta} - 1 \right) \cdot \Delta t \cdot \ddot{u}_t \right] \cdot C$$

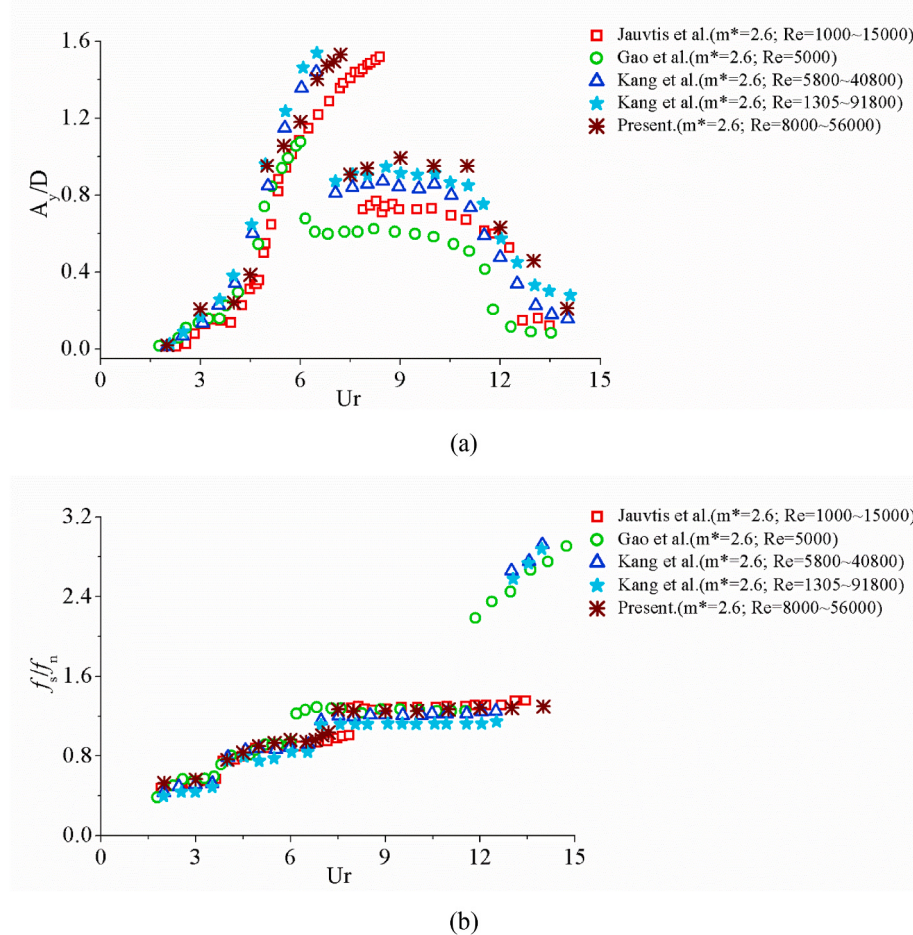


**Fig. 6.** The validation of numerical model: (a) the validation of amplitude; and (b) the validation of frequency.

$\Delta t$  is the time step.

The above equations are solved using the C language, and the C language algorithms are written in UDF. In order to solve the fluid force acting on the structure, 2D-RANS equations and SST/ $k-\omega$  turbulence model are adopted in Fluent. Then, the acceleration, velocity and displacement of the structure are solved in UDF. Finally, the mesh of the computational domain is updated based on new motion state. Fig. 3 shows the process of numerical calculation.

### 3.2. The validation of mesh dependence

Fig. 4 shows the computational domain, which includes four sub-regions (*External Flow Field*, *Sub-Domain*, *X-Slipway* and *Y-Slipway*). The range of this domain is  $60D$  (length) in the in-flow direction and  $40D$  (width) in the cross-flow direction, and the blocking ratio is 0.025. The blocking ratio is  $W/D$ , and  $W$  is the width ( $40D$ ) in the cross-flow direction. When  $W/D$  is less than 0.05, the influence of the width of the computational domain on the numerical calculation is less (Gao et al., 2018). The ranges of four sub-regions are set as shown in Fig. 4. The boundary conditions are set as follows. The “Inlet” is the velocity inlet ( $u = U$ ,  $v = 0$ ), the “Outlet” is the outflow ( $\partial u / \partial x = 0$ ,  $\partial v / \partial x = 0$ ), and the “Side-Wall” is the symmetry boundary ( $\partial u / \partial y = 0$ ,  $v = 0$ ). The mesh is updated using the Layer-Method and the specific steps of this method have been shown in the author’s previous papers (Wang et al., 2019(b); Wang et al., 2019(c); Wang et al., 2020).

The moving boundary is described by an Arbitrary Lagrangian–Eulerian (ALE) scheme, which makes the computational mesh

around the structure moving along with the VIV system (Wang et al., 2019(c)). The interfaces are adopted to connect the different mesh regions. The Sub-domain and Cylinder-wall move up and down together. The Sub-domain, Y-slipway, X-slipway and External flow field are tessellated with different shapes of meshes. The Y-slipway, X-slipway and External flow field are meshed with quadrilateral grids. The Sub-domain is meshed with triangular grids. The boundary layer meshes around the cylinder are quadrilateral grids to improve the accuracy on resolving the flow around the structure. The layers of boundary layer mesh are 25 and the growth ratio of boundary-layer mesh is 1.05. The height of the first layer is determined by  $y^+$ , which is expressed as:

$$y^+ = 0.172 \frac{\Delta y}{D} Re^{0.9} \quad (14)$$

where  $\Delta y$  is height of the first-layer mesh. Based on the previous research (Wang et al., 2019(c)),  $y^+$  is less than 1.

The mesh has a greater impact on the results of numerical calculations, so the mesh dependence needs to be verified. Five different mesh densities are shown in Table 2, including  $3.0 \times 10^4$  (Q1),  $6.0 \times 10^4$  (Q2),  $9.0 \times 10^4$  (Q3),  $1.2 \times 10^5$  (Q4) and  $1.5 \times 10^5$  (Q5). The percentage in brackets is the comparison of this mesh to the previous mesh. When the differences of  $A_y/D$  and  $f_s/f_n$  between the two meshes are less than 0.1%, the influence of the mesh on the calculation results can be negligible (Gao et al., 2018). The mesh changes from Q4 to Q5, the difference percentages of  $A_y/D$  and  $f_s/f_n$  are 0.05% and 0.04%. Therefore, the mesh Q5 can be adopted, and Fig. 5 shows the meshes.

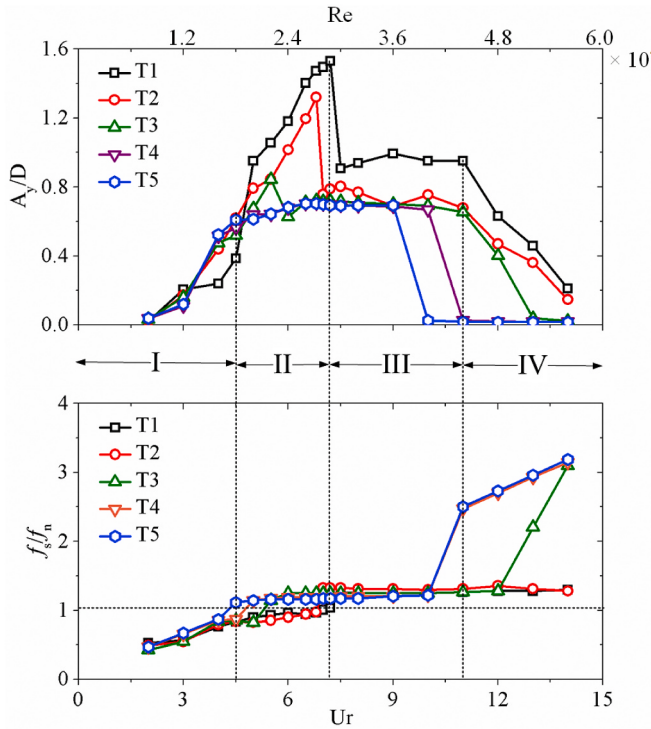


**Fig. 7.** The amplitude responses and the frequency responses of the five cylinders.

### 3.3. The validation of numerical model

The experimental data (Jauvtis and Williamson, 2004) and the similar numerical data (Gao et al., 2018; Kang et al., 2019) are referenced to verify the accuracy of the numerical methods in this paper. The range of reduced velocity is  $2 < U_r (U_r = \frac{U}{f_n D}) < 14$ , and the results of the numerical model verification are shown in Fig. 6. The Fast Fourier Transform (FFT) of lift coefficient can get vortex shedding frequency ( $f_s$ ).

Jauvtis and Williamson used three branches to distinguish the VIV response region, which are the initial branch ( $U_r \leq 4.0$ ), the upper branch ( $4 < U_r < 8.0$ ), and the lower branch ( $U_r \geq 8.0$ ) (Jauvtis and Williamson, 2004). From the upper branch to the lower branch, the amplitude ratio decreases abruptly, while the frequency ratio increases abruptly. The reduced velocity where this phenomenon occurs is at  $6 < U_r < 8$  (Jauvtis and Williamson, 2004). This phenomenon is also observed at  $U_r \approx 7.0$  in this paper. Obviously, there are some differences between the results of the numerical model in this paper and results in the experiment (Jauvtis and Williamson, 2004). The possible reasons are the differences in Reynolds number. The reason for the difference of Reynolds number in this paper is that the diameter of cylinder is larger than that in experiment, and the velocity range is the same for them. The  $U_r$  is calculated by the change of  $f_n$  in the Gao's numerical model (Gao et al., 2018), and the Reynolds number fixed at 5000. In numerical verification, the Reynolds number or the reduced velocity can be selected in the expression of  $x$ -coordinate. Because the Reynolds number cannot be exactly the same, the expression of  $x$ -coordinate in Fig. 6 selects the reduced velocity. The numerical solution in this paper can clearly show three branches and the lock-in region can also be clearly shown. Compared with the prediction accuracy of amplitude response, the prediction accuracy of frequency response is higher. The frequency ratio response is in good agreement with that in the experiment (Jauvtis and Williamson, 2004). The  $U_r$  is calculated by the change of  $U$  in the Jauvtis's experimental model (Jauvtis and Williamson, 2004), Kang's numerical model (Kang et al., 2019) and the numerical model in this paper. Two different ranges of Reynolds number were provided in

Kang's model, including  $5.8 \times 10^3 \leq Re \leq 4.08 \times 10^4$  and  $1.305 \times 10^3 \leq Re \leq 9.18 \times 10^4$ . The amplitude ratio response is in good agreement with that in Kang' studies (Kang et al., 2019). Therefore, the numerical scheme in this paper is acceptable.

## 4. Results and discussion

### 4.1. Cylinder response

The cross-flow amplitude responses and the vortex shedding frequency responses of the cylinders with the bionic surfaces of five different height ratios ( $K_s/D$ ) are shown in Fig. 8. When the vortex shedding frequency ( $f_s$ ) approaches the natural frequency ( $f_n$ ) of the structure, the lock-in of VIV response occurs (Jauvtis and Williamson, 2004). The vortex shedding frequency ( $f_s$ ) of VIV response is obtained by Fast Fourier Transform (FFT) of the lift force. For a large-mass-ratio structure ( $m^* = O(100)$ ) in air, the lock-in occurs when  $f_s/f_n \approx 1.0$ , and the range of the lock-in region is very small (Feng, 1968). However, the range of lock-in region for a low-mass-ratio structure ( $m^* = O(10)$ ) is lager in water (Khalak and Williamson, 1999) compared with that in air. The natural frequency of the structure is the frequency in still water. The flow around the structure is changed when the structure vibrates, and the additional mass also has a greater impact on a low-mass-ratio structure in water (Jauvtis and Williamson, 2004). Therefore, the lock-in still occurs when  $f_s/f_n$  is far from 1, and this phenomenon is more clearly observed in water when the mass-ratio is smaller (Wang et al., 2019(c)). The VIV response region is usually divided into three branches (Khalak and Williamson, 1999), including a lock-in region (the upper branch) and two other regions (the initial branch and the lower branch). In order to show the lock-in region more clearly, the lock-in region is divided into two in Fig. 7. The VIV response region is divided into four regions, as shown in Table 3.

In region I, the frequency ratios of the different cylinders show a rapid upward trend, and the frequency ratios are less than 1.0. The amplitude ratios also show a rapid upward trend, and the maximum amplitude ratios are about 0.6. The amplitude ratios of T2, T3, T4 and T5 is more than that of T1 when  $3.0 < U_r < 4.5$ .

In region II, the frequency ratios of T1, T2, T3, T4 and T5 are close to 1.0 and then more than 1.0. However, the frequency ratio of T5 is more than 1.0 at  $U_r = 4.5$ , the frequency ratio of T4 is more than 1.0 at  $U_r = 5.0$ , the frequency ratio of T3 is more than 1.0 at  $U_r = 6.0$ , and the frequency ratio of T1 and T2 is more than 1.0 at  $U_r = 7.0$ . The lock-in phenomenon gradually occurs in advanced as the height ratio of the bionic surface increases. The amplitude ratios show a rapid upward trend for T1, T2 and T3. The amplitude ratio of T1 reaches the maximum value of 1.5 at  $U_r = 7.0$ , the amplitude ratio of T2 reaches the maximum value of 1.3 at  $U_r = 6.5$  and the amplitude ratio of T3 reaches the maximum value of 0.9 at  $U_r = 5.5$ . For T4 and T5, the amplitude ratios are less than 8.0 and the amplitude ratio changes gently. The maximum cross-flow amplitude ratio decreases from 1.5 (T1) to 0.75 (T5), which reduces by about 50%.

In region III, the frequency ratios of the different cylinders are more than 1.0, and near a more stable value. Therefore, they are in a stable lock-in region. For T4 and T5, the amplitude ratios are similar to that in region II, and they do not increase and remains stability. However, the amplitude ratios of T1, T2 and T3 reduce first and then remains stability. The stable amplitude ratio of T1 is about 1.0 and the stable amplitude ratios of T2, T3, T4 and T5 are about 0.8.

In region IV, the amplitude ratios begin to decrease rapidly. However, the amplitude ratios of T1, T2 and T3 begin to decrease at  $U_r = 11.0$ , the amplitude ratio of T4 begins to decrease at  $U_r = 10.0$  and the amplitude ratio of T5 begins to decrease at  $U_r = 9.0$ . At the same time, the jump of frequency ratios for T4 and T5 occurs when  $U_r = 10-11$ . Obviously, the range of the lock-in region is smaller for T4 and T5 compared with that of T1. As reduced velocity ( $U_r$ ) increases, the cross-flow amplitude ratios of T4 and T5 are about 0.0.

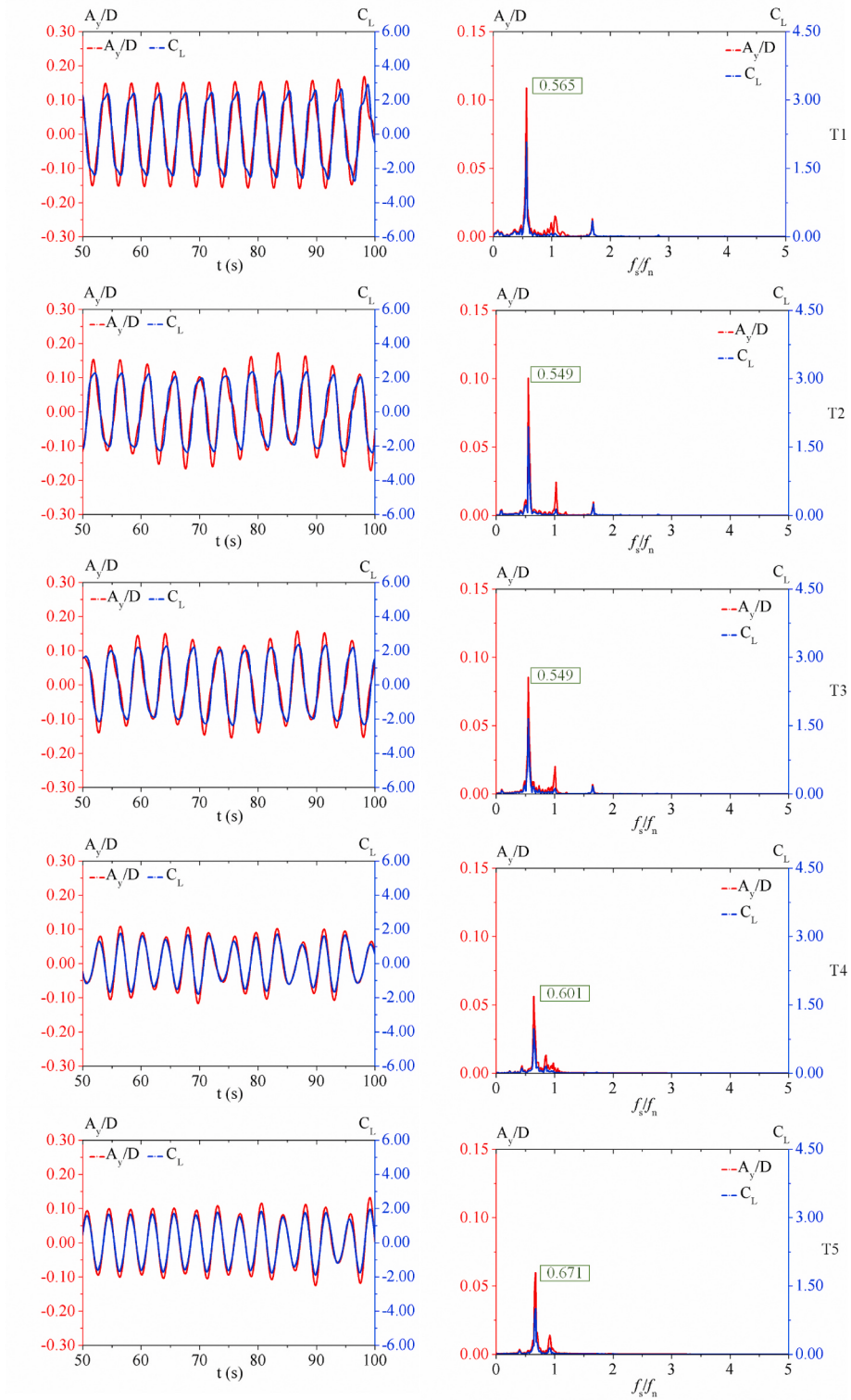


**Fig. 8.** VIV responses of five different cylinders ( $U_r = 3.0$ ,  $Re = 1.2 \times 10^4$ ).

Figs. 8–11 show the time histories of VIV responses, and four typical reduced velocities ( $U_r = 3.0, 6.0, 9.0$  and  $13.0$ ) are selected based on the VIV response region. Fig. 8 shows the time histories of VIV responses when  $U_r = 3.0$  ( $Re = 1.2 \times 10^4$ ) in region I. In region I, the amplitude ratios and frequency ratios of T1, T2 and T3 are similar. The maximum cross-flow amplitude ratios of T1, T2 and T3 are about 0.15. The maximum cross-flow amplitude ratios of T4 and T5 are about 0.10. The frequency ratios of T2 and T3 are less than that of T1, and the frequency

ratios of T4 and T5 are more than that of T1. Fig. 9 shows the time histories of VIV responses when  $U_r = 6.0$  ( $Re = 2.4 \times 10^4$ ) in region II. In region II, the frequency ratios of T1 and T2 are near 1.0, but they are less than 1.0. However, the frequency ratios of T3, T4 and T5 are more than 1.0. The frequency spectrum of the lift coefficient has two peaks. The maximum amplitude ratio of T1 are about 1.2, the maximum amplitude ratio of T2 is about 1.1, and the maximum amplitude ratios of T3, T4 and T5 are about 0.75. Fig. 10 shows the time histories of VIV responses

**Table 3**  
VIV response regions.

Case	Region I	Region II	Region III	Region IV	Lock-in range
T1	1.0–4.0	4.5–7.0	7.5–11.0	11.5–14.0	6.5
T2	1.0–4.0	4.5–6.5	7.0–11.0	11.5–14.0	6.5
T3	1.0–4.0	4.5–5.5	6.0–11.0	11.5–14.0	6.5
T4	1.0–4.0	4.5–5.5	6.0–10.0	10.5–14.0	6.0
T5	1.0–3.5	4.0–5.0	5.5–9.0	9.5–14.0	5.0

when  $U_r = 9.0$  ( $Re = 3.6 \times 10^4$ ) in region III. In region III, the frequency ratio of T1 is more than 1.0, and the frequency spectrum of the lift coefficient has two peaks. The frequency ratios of T2, T3, T4 and T5 are also more than 1.0, and the frequency spectrum of lift coefficient has three peaks. The appearance of multi peaks is related to the bionic surface, which may change the flow around the cylinder. The maximum cross-flow amplitude ratio of T1 is about 1.0, and they are about 0.75 for T2, T3, T4 and T5. Fig. 11 shows the time histories of VIV responses when  $U_r = 13.0$  ( $Re = 5.2 \times 10^4$ ) in region IV. In region IV, the frequency ratios of T1, T2, T3, T4 and T5 are far away from 1.0. The frequency spectrum of the lift coefficient has two peaks for T1 and T2. However, the frequency spectrum of amplitude ratio is lower than that of the lift coefficient for T3, and the frequency spectrum of the lift coefficient is about twice that of the amplitude ratio. The main peak values of frequency spectrum of the lift coefficient and the amplitude ratio coincide again for T4 and T5. But the main peak values of frequency spectrum of T4 and T5 are more than that of T1. VIV responses of T4 and T5 are characterized by the high frequency ratio and the low amplitude ratio in region IV.

#### 4.2. Vortex force and vortex pattern

In order to better analyze the frequency spectrum of the lift coefficient in Section 4.1, the lift force coefficient is further analyzed and vortex pattern is analyzed. The total lift force consists of the vortex force ( $F_{\text{vortex}}$ ) and the potential force ( $F_{\text{potential}}$ ). The vortex force is caused by the vortex shedding and the potential force is caused by the potential added-mass force (Govardhan and Williamson, 2000). Obviously, the vortex force is related to the vortex pattern. The total lift force can be expressed as:

$$F_y(t) = F_{\text{vortex}}(t) + F_{\text{potential}}(t) \quad (15)$$

Normalizing all the forces by  $(\rho U^2 DL/2)$ , Eq. (15) can be expressed as:

$$C_y(t) = C_{\text{vortex}}(t) + C_{\text{potential}}(t) \quad (16)$$

where  $C_{\text{potential}}(t)$  can be expressed as:

$$C_{\text{potential}}(t) = 2\pi^3 \frac{\left[ \frac{A_y(t)}{D} \right]}{\left[ \frac{U}{f_s D} \right]^2} \quad (17)$$

in which  $A_y(t)$  is the vibrate amplitude in cross-flow direction,  $f_s$  is the vortex shedding frequency.  $C_{\text{potential}}(t)$  is always in phase with  $A_y(t)$ .

The total lift force coefficients, the vortex force coefficients, the potential force coefficients and the vortex patterns of five different cylinders are shown in Figs. 12–15. The vorticity is defined as  $\omega = \partial u / \partial y - \partial v / \partial x$ . Fig. 12 shows the time histories of the total lift force coefficients, the vortex force coefficients, the potential force coefficients and the vortex patterns of five different cylinders when  $U_r = 3.0$  ( $Re = 1.2 \times 10^4$ ) in region I. In region I, the vortex force coefficients, the potential force coefficients of T1, T2, T3, T4 and T5 are in phase. The relationship between the total lift force coefficient ( $C_L(t)$ ) and the vortex force coefficient ( $C_{\text{vortex}}(t)$ ) is  $C_L(t) \approx C_{\text{vortex}}(t)$ , so the total lift force mainly comes from the vortex force for T3, T4 and T5. The potential force coefficients of T3, T4 and T5 are very small, so the cross-flow vibrate amplitudes are very small. The vortex force coefficients of T3, T4 and T5 are smaller than that of T1 and T2. Therefore, the bionic surface can well suppress the VIV response. The vortex patterns of T1, T2, T3, T4 and T5 are all 2S modes in this region.

T4 and T5 are 2S modes, and 2S mode means that two vortices shed in each cycle. 2S mode is similar to “Carmen Vortex”, and this phenomenon also appeared in the experiments of Khalak and Williamson (1999). The potential force coefficient is very small, so the cross-flow vibrate amplitude is very small. The maximum potential force coefficients of T4 and T5 are slightly smaller than that of T1, T2 and T3.

Fig. 13 shows the time histories of the total lift force coefficients, the vortex force coefficients, the potential force coefficients and the vortex patterns of five different cylinders when  $U_r = 6.0$  ( $Re = 2.4 \times 10^4$ ) in region II. In region II, the total lift force coefficients and the potential force coefficients of T1 and T2 are out of phase. At the same time, the vortex force coefficients of T1 and T2 have two peaks, which is why the two peaks appears in Fig. 9. The phase differences between the potential force coefficients and the vortex force coefficients for T3, T4 and T5 are close to  $\pi$ . Therefore, the total lift force coefficients of T3, T4 and T5 decrease obviously and the bionic surface improves the flow characteristics around the cylinder. The vortex patterns of T1 and T2 are still 2S modes, but the vortex patterns of T3, T4, and T5 are 2P modes. 2P mode means that two vortices shed from each side of the cylinder in each half cycle.

Fig. 14 shows the time histories of the total lift force coefficients, the vortex force coefficients, the potential force coefficients and the vortex patterns of five different cylinders when  $U_r = 10.0$  ( $Re = 4.0 \times 10^4$ ) in region III. In region III, the phase differences between the potential force coefficients and the vortex force coefficients for T1, T2, T3, T4 and T5 are all about  $\pi$ . With the increase of the height ratio of the bionic surface, the vortex force coefficients and the potential force coefficients decrease gradually. The vortex pattern of T1 is 2P mode, but the vortex patterns of T2, T3, T4 and T5 are P + S modes. P + S mode means that three vortices shed in each cycle, and two vortices shed from one side of the cylinder and only one vortex shed from other side of the cylinder. In the lock-in region, the strength of vortices increases, and the effect on the cylinder also increases. The vortex mode is more complex in the lock-in region.

Fig. 15 shows the time histories of the total lift force coefficients, the vortex force coefficients, the potential force coefficients and the vortex patterns of five different cylinders when  $U_r = 13.0$  ( $Re = 5.2 \times 10^4$ ) in region IV. In region IV, the total lift force coefficients and the potential force coefficients of T1 and T2 are out of phase. However, the vortex force coefficients and the potential force coefficients of T3, T4 and T5 are in phase. The relationship between the total lift force coefficient ( $C_L(t)$ ) and the vortex force coefficient ( $C_{\text{vortex}}(t)$ ) is  $C_L(t) \approx C_{\text{vortex}}(t)$ , so the total lift force mainly comes from the vortex force for T3, T4 and T5. The potential force coefficients of T3, T4 and T5 are very small, so the cross-flow vibrate amplitudes are very small. The vortex force coefficients of T3, T4 and T5 are smaller than that of T1 and T2. Therefore, the bionic surface can well suppress the VIV response. The vortex patterns of T1, T2, T3, T4 and T5 are all 2S modes in this region.

#### 4.3. Frequency ratio and vortex phase

In order to understand the transition of vortex pattern, the vortex phase between the vortex force and the cross-flow amplitude ratio based on the vortex shedding frequency ratio ( $f_s/f_n$ ). The vortex phase can be expressed as (Govardhan and Williamson, 2000):

$$\tan \varphi_{\text{vortex}} = \frac{2 \cdot \xi \cdot f_s / f_n}{1 - \left( \frac{f_s}{f_n} \right)^2} \quad (18)$$

where  $\varphi_{\text{vortex}}$  is the vortex phase. The vortex phases of five different cylinders are shown in Fig. 16.

For a smooth cylinder (T1,  $K_s/D = 0.0$ ), the vortex pattern is 2S mode in region I, region II, and region IV. The jump of frequency ratio occurs between region II and region III, and the vortex pattern is 2P mode in region III. In region I and region II, the frequency ratio is near 1.0, but it is not more than 1.0. When the frequency ratio is more than 1.0, the

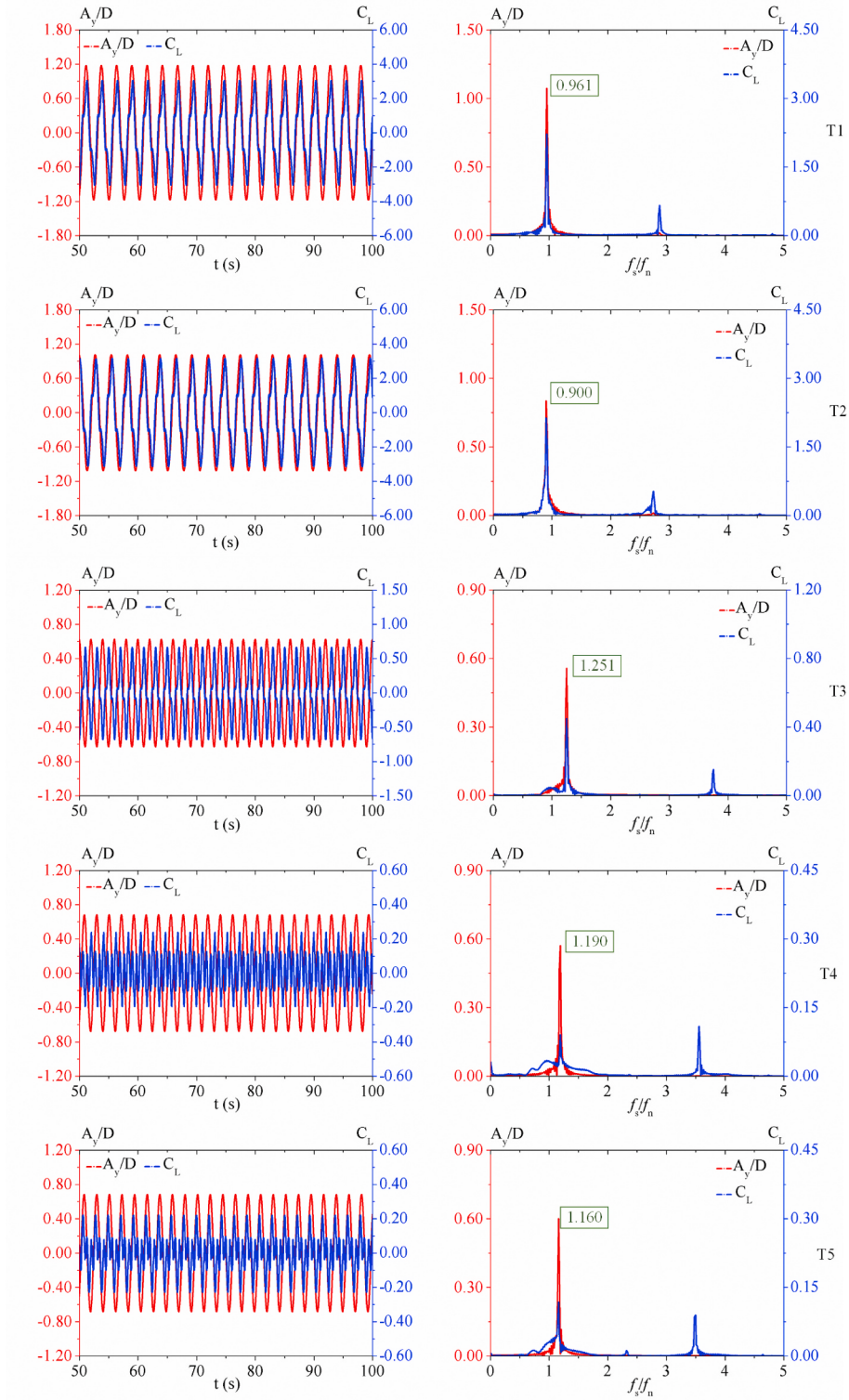


**Fig. 9.** VIV responses of five different cylinders ( $U_r = 6.0$ ,  $Re = 2.4 \times 10^4$ ).

jump of frequency ratio occurs and the vortex phase jump from about  $0^\circ$  to about  $180^\circ$ . In this process, the phase difference between the vortex force coefficients and the potential force coefficients jumps from 0 to  $\pi$ .

For T2 ( $K_s/D = 0.025$ ), the vortex pattern is 2S mode in region I, region II, and region IV. The jump of frequency ratio occurs between region II and region III, and the vortex pattern is P + S mode in region III. The vortex force coefficient of T2 is smaller than that of T1, and the vortex pattern is changed because of the bionic surface. For T3 ( $K_s/D =$

0.050), T4 ( $K_s/D = 0.075$ ) and T5 ( $K_s/D = 0.100$ ), the vortex patterns are 2S modes in region I and region IV. However, the vortex patterns are 2P modes in region II and they are P + S modes in region III. The jump of frequency ratio occurs between region I and region II for T3, T4 and T5. Therefore, the jump of frequency ratio occurs earlier for T3, T4 and T5 compared with that for T1 and T2. It can be seen from Fig. 16 that the jump of the frequency ratio gradually occurs earlier as the height ratio increases.

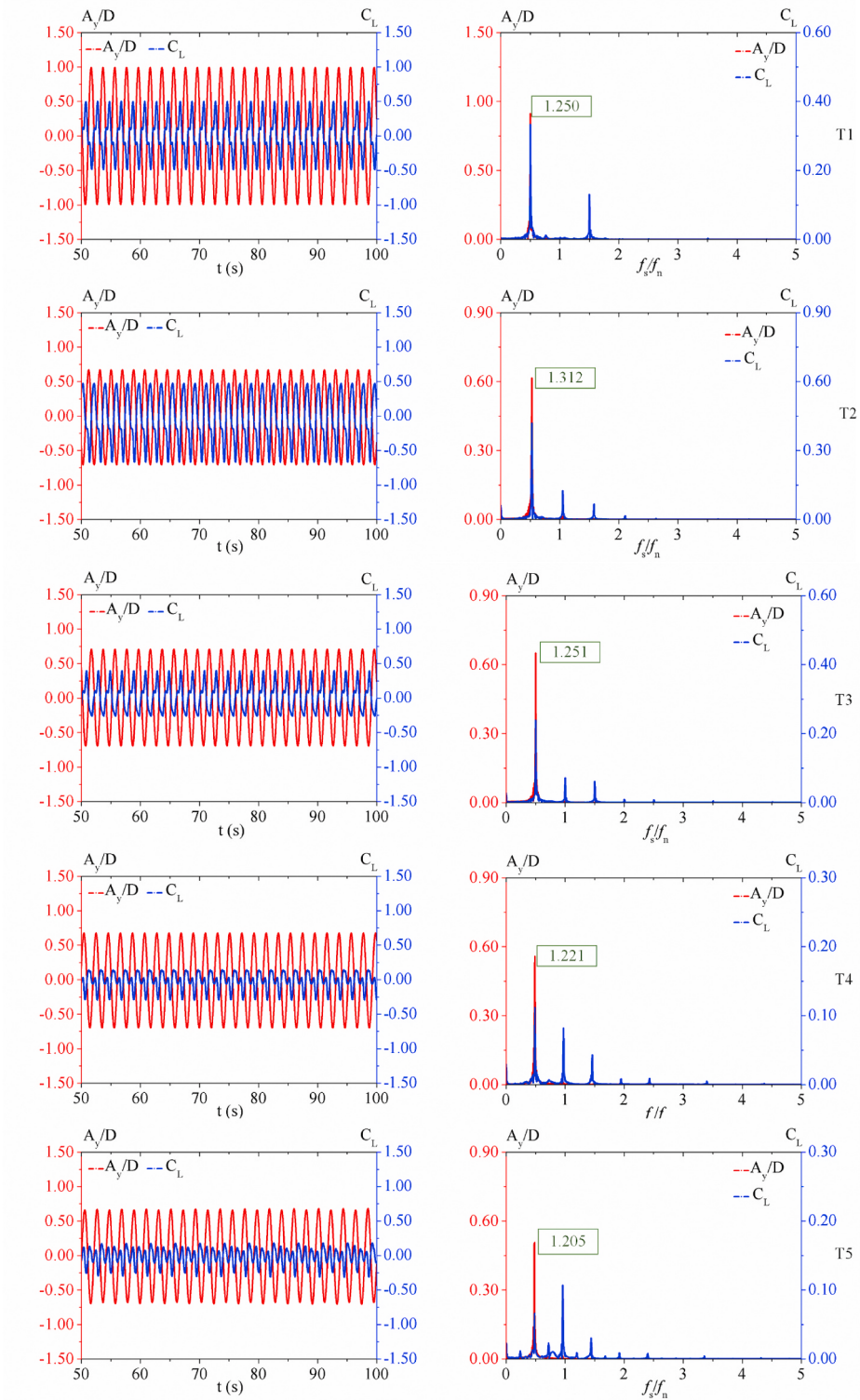


**Fig. 10.** VIV responses of five different cylinders ( $U_r = 9.0$ ,  $Re = 3.6 \times 10^4$ ).

#### 4.4. General discussion

The in-line amplitude responses of the cylinders with different bionic surfaces are shown in Fig. 17. The in-line amplitude response of a smooth cylinder was studied in the Jauvtis and Williamson's experiments (Jauvtis and Williamson, 2004), which is referenced in Fig. 17. T1 is also a smooth cylinder, and the in-line amplitude ratio of T1 are good agree with that of Jauvtis and Williamson's experiments (Jauvtis and

Williamson, 2004). In region I, the in-line amplitude ratios of T1 and T2 have similar trends, increasing first and then decreasing. The change trends of T4 and T5 are opposite to that of T1 and T2, and the possible causes are that the bionic surfaces change the flow around the structure. The in-line amplitude ratios are less than 0.2. In region II, the fluctuation trends of T1, T2 and T3 are similar, which show an upward trend. The maximum in-line amplitude ratios of T1, T2 and T3 are approximately 0.35 at  $U_r = 7.0$ , 0.22 at  $U_r = 6.8$  and 0.20 at  $U_r = 5.5$ . However, the

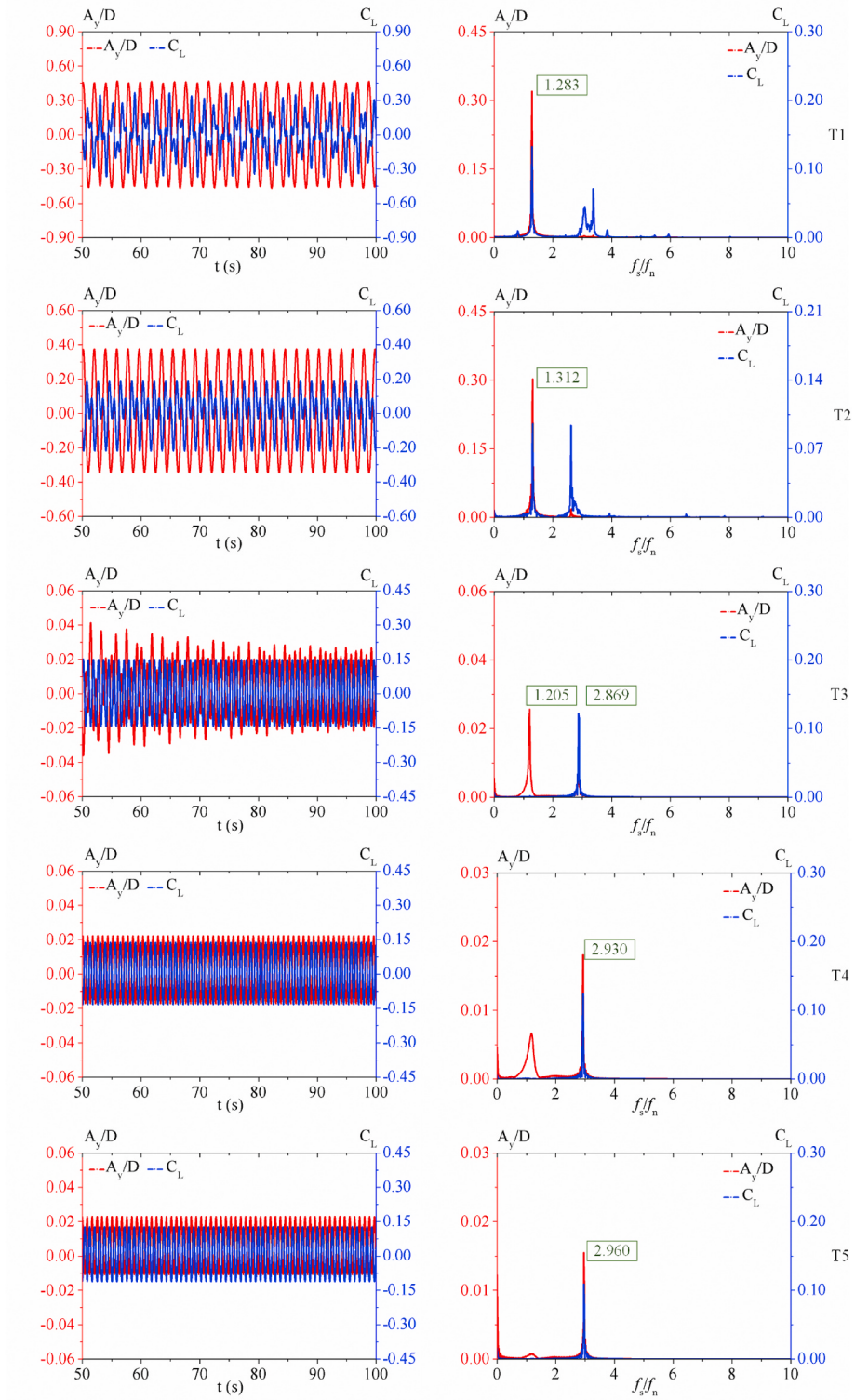
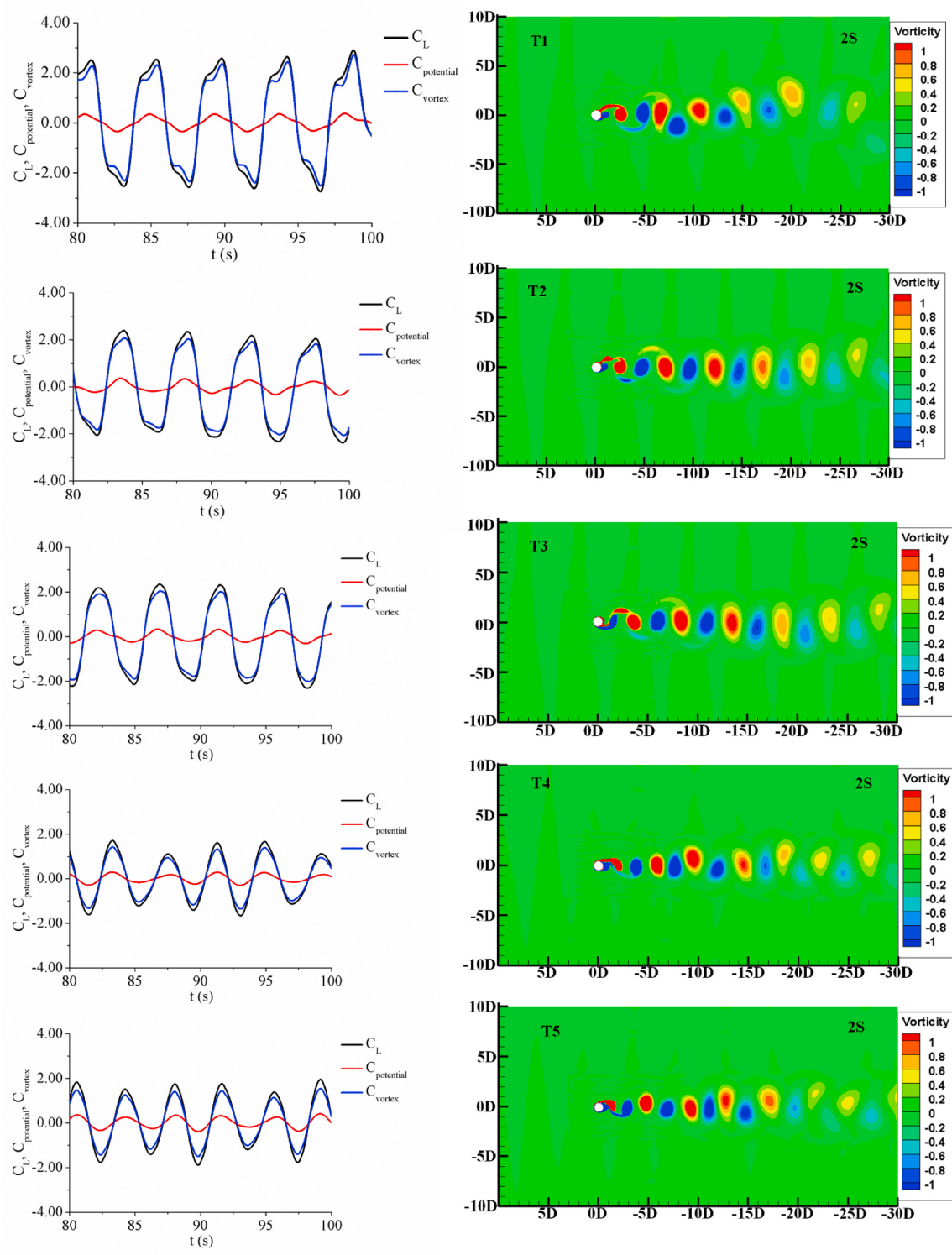


Fig. 11. VIV responses of five different cylinders ( $U_r = 13.0$ ,  $Re = 5.2 \times 10^4$ ).

maximum in-line amplitude ratios of T4 and T5 are about 0.16 at  $U_r = 4.0$  and 0.12 at  $U_r = 4.0$ . The in-line amplitude ratios of T4 and T5 decrease rapidly in region II and then keep at a stable value, which is about 0.025. In region III, the in-line amplitude ratios of T4 and T5 are reduced to about 0.0. The in-line amplitude ratios of T1, T2 and T3 decrease rapidly, and the maximum in-line amplitude ratios are less than 0.1. In region IV, because VIV response is far away the lock-in region, the in-line amplitude ratios of T1, T2, T3, T4 and T5 are very small. The

following conclusions can be drawn based on the above analysis: 1) As the height ratios of the bionic surface increase, the maximum in-line amplitude ratios gradually decrease; 2) As the height ratios of the bionic surface increase, the range of the large-amplitude-motion region gradually decreases; 3) As the height ratios of the bionic surface increase, the maximum in-line amplitude ratio occurs earlier; 4) The maximum in-line amplitude ratio decreases from 0.35 (T1) to 0.12 (T5), which reduces by about 65.7%.



**Fig. 12.** The total lift force coefficients ( $C_L$ ), the vortex force coefficients ( $C_{\text{vortex}}$ ), the potential force coefficients ( $C_{\text{potential}}$ ) and the vortex patterns of five different cylinders ( $U_r = 3.0$ ,  $\text{Re} = 1.2 \times 10^4$ ).

The mean drag coefficients of the cylinders with different bionic surfaces are shown in Fig. 18. In region I, the mean drag coefficients of T1, T2 and T3 have similar trends, increasing first and then decreasing. The change trends of T4 and T5 are opposite to that of T1, T2 and T3. This phenomenon results the same fluctuation trends of the in-line amplitude ratios. When  $U_r < 3.0$ , the mean drag coefficients and the in-line amplitude ratios of T1, T2 and T3 show an upward trend, which

was observed in Jauvtis and Williamson's experiments (Jauvtis and Williamson, 2004). In region II, the fluctuation trends of T1, T2, T3, T4 and T5 are similar, showing an upward trend. The maximum mean drag coefficients of T1, T2, T3, T4 and T5 are 3.0 at  $U_r = 7.0$ , 3.0 at  $U_r = 6.8$ , 2.5 at  $U_r = 5.5$ , 2.3 at  $U_r = 5.0$  and 2.25 at  $U_r = 4.5$ . As the height ratios of the bionic surface increase, the maximum mean drag coefficient occurs gradually earlier. The mean drag coefficients of a stationary

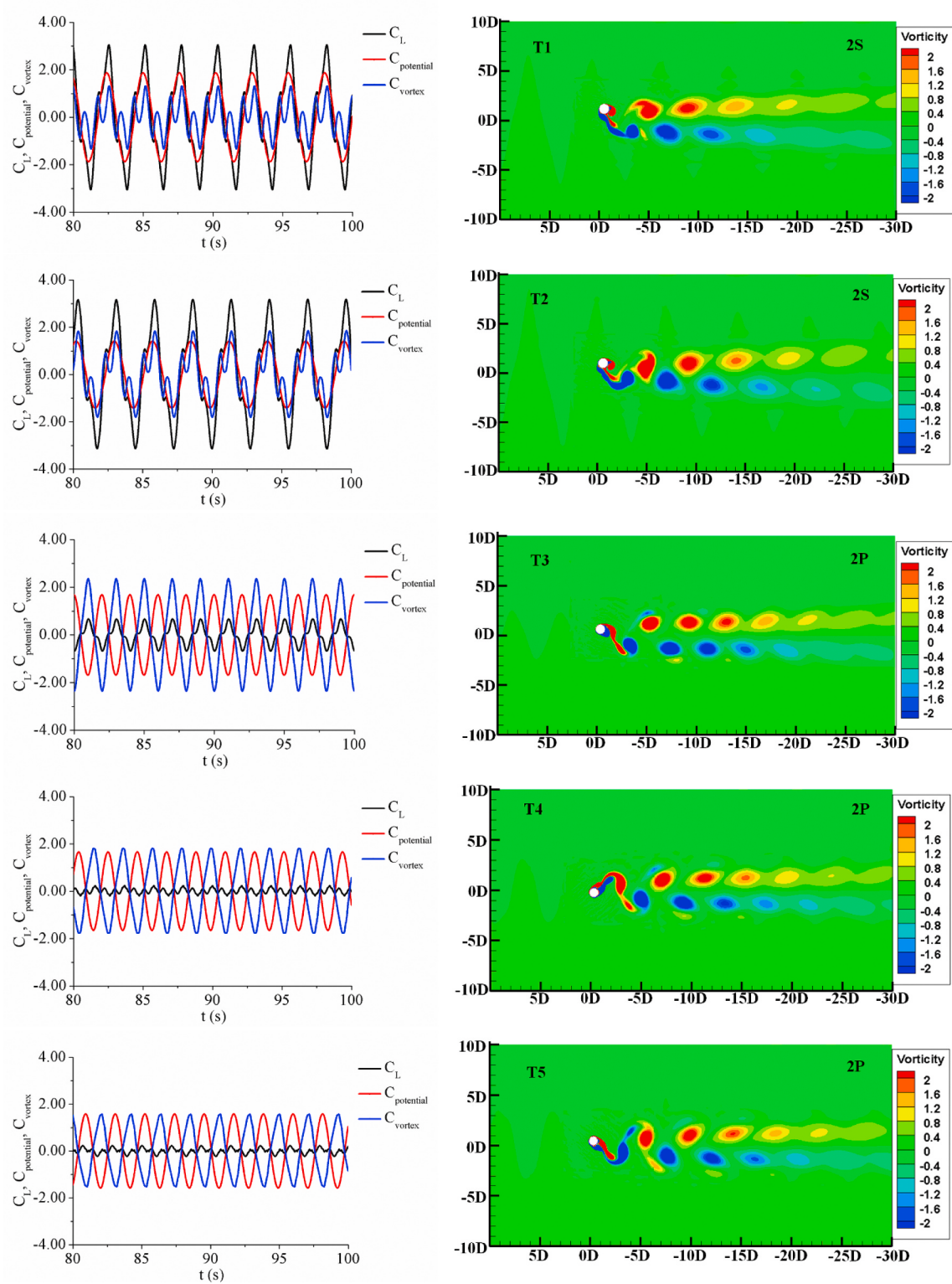


**Fig. 13.** The total lift force coefficients ( $C_L$ ), the vortex force coefficients ( $C_{\text{vortex}}$ ), the potential force coefficients ( $C_{\text{potential}}$ ) and the vortex patterns of five different cylinders ( $U_r = 6.0$ ,  $\text{Re} = 2.4 \times 10^4$ ).

cylinder is about 1.0 in this Reynolds number range (Jauvitis and Williamson, 2004; Zhu et al., 2017). And the maximum mean drag coefficient of the bare cylinder is about 3.0, which has a threefold increase over that of the stationary cylinder. The similar phenomenon has been also observed in previous studies (Jauvitis and Williamson, 2004; Zhu et al., 2017). Due to the vortex-induced vibration response of the bare

cylinder, the peak mean drag coefficient of the structure is quite large when the vibration amplitude is very large in the lock-in region. However, the mean drag coefficient of the bare cylinder in VIV response region is close to that of the stationary cylinder when the vibration amplitude is very low. In region III, the mean drag coefficients of T1, T2, T3, T4 and T5 show a downward trend. In region IV, the mean drags

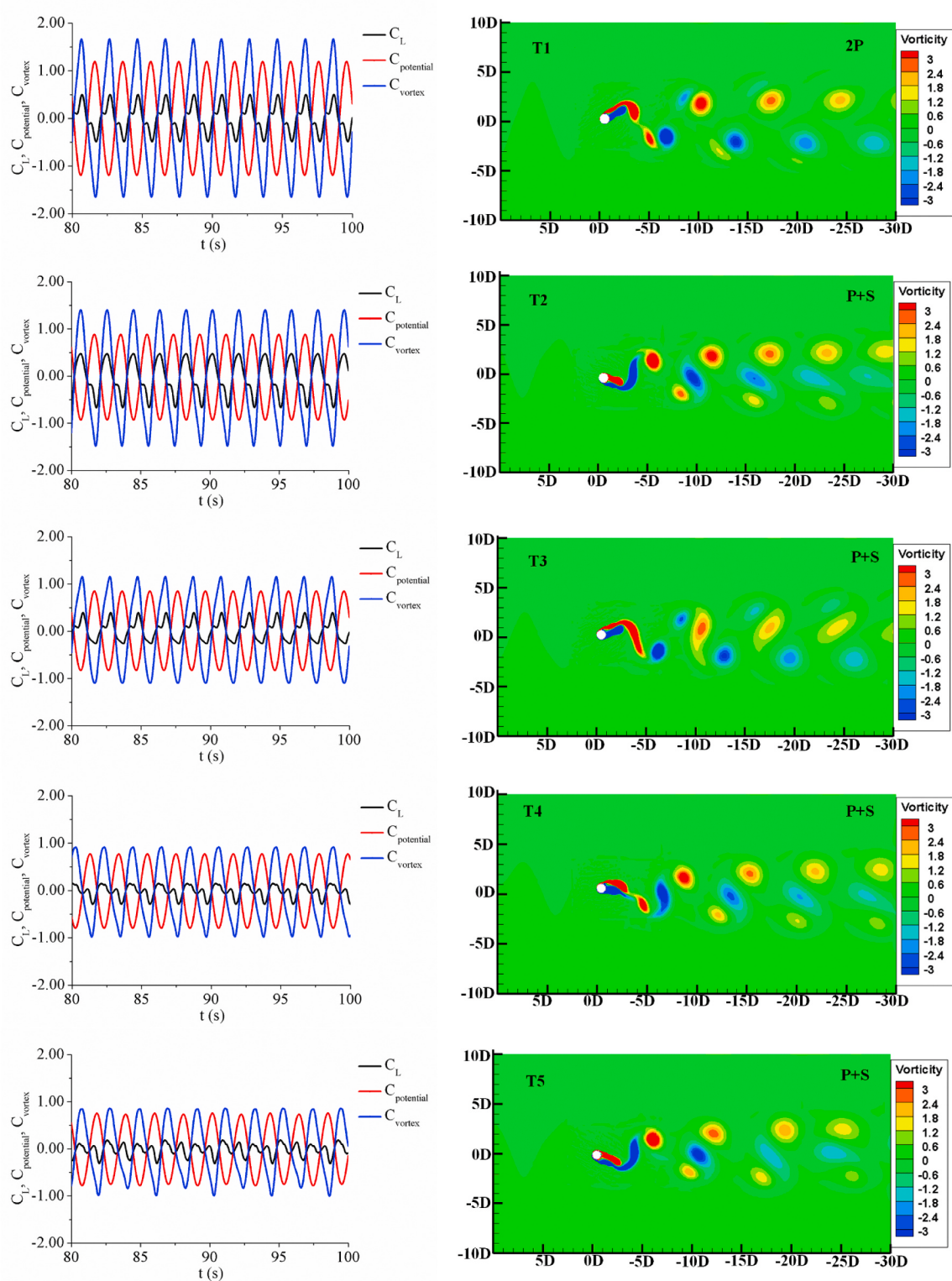


**Fig. 14.** The total lift force coefficients ( $C_L$ ), the vortex force coefficients ( $C_{\text{vortex}}$ ), the potential force coefficients ( $C_{\text{potential}}$ ) and the vortex patterns of five different cylinders ( $U_r = 10.0$ ,  $\text{Re} = 4.0 \times 10^4$ ).

coefficients of T1, T2, T3, T4 and T5 keep at a low value. In particular, the mean drag coefficient of T5 is reduced to about 0.8 at  $U_r = 10.0$ . The maximum drag coefficient decreases from 3.0 (T1) to 2.25 (T5), which reduce by about 25%.

The motion trajectories of the cylinders with different bionic surfaces are shown in Fig. 19. The typical motion trajectory of eight-shaped is observed for T1. However, as  $U_r$  increases, the size of eight-shaped

increases first and then decreases. The range of eight-shaped figure for T1 is  $[-0.01\text{m} \leq A_x \leq 0.01\text{m}; -0.002\text{m} \leq A_y \leq 0.002\text{m}]$  at  $U_r = 2.0$ , the range of eight-shaped figure is  $[0.02\text{m} \leq A_x \leq 0.06\text{m}; -0.12\text{m} \leq A_y \leq 0.12\text{m}]$  at  $U_r = 6.0$  and the range of eight-shaped figure is  $[0.063\text{m} \leq A_x \leq 0.075\text{m}; -0.09\text{m} \leq A_y \leq 0.09\text{m}]$  at  $U_r = 12.0$ . As  $U_r$  increases, the in-line vibration displacement increases. And the central location of the in-line vibration is about  $-0.005\text{m}$  for T1 at  $U_r = 2.0$ ,  $0.030\text{ m}$  at  $U_r = 6.0$ ,

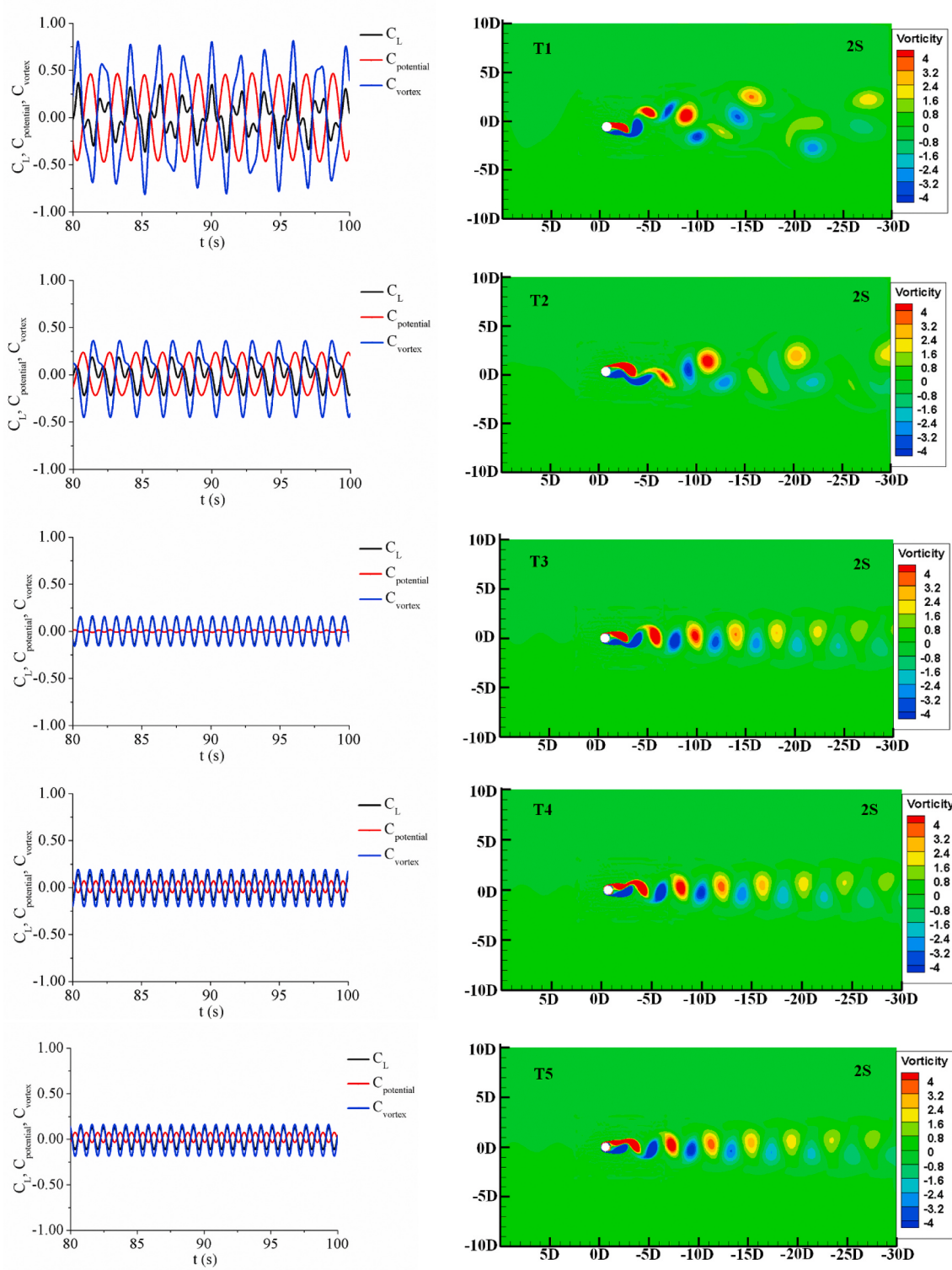


**Fig. 15.** The total lift force coefficients ( $C_L$ ), the vortex force coefficients ( $C_{\text{vortex}}$ ), the potential force coefficients ( $C_{\text{potential}}$ ) and the vortex patterns of five different cylinders ( $U_r = 13.0$ ,  $\text{Re} = 5.2 \times 10^4$ ).

0.066 m at  $U_r = 12.0$ . For T2, the motion trajectories are ellipse-shaped at  $U_r = 2.0$ , eight-shaped at  $U_r = 6.0$ , and raindrop-shaped at  $U_r = 12.0$ . For T3, the motion trajectories are disordered at  $U_r = 2.0$ , eight-shaped at  $U_r = 6.0$ , and eight-shaped at  $U_r = 12.0$ . For T4 and T5, the motion trajectories are eight-shaped at  $U_r = 2.0$ , eight-shaped at  $U_r = 6.0$ , and line-shaped at  $U_r = 12.0$ . When  $U_r = 6.0$  (lock-in region), the motion trajectories of T1, T2, T3, T4 and T5 are all the eight-shaped, but the

ranges of motion trajectories are smaller for T4 and T5 compared with that of T1. In particular, the in-line amplitude of T4 and T5 is close to 0 at  $U_r = 12.0$ .

#### 4.5. Discussion on control mechanism of the bionic surface

In Sections 4.1, 4.2, 4.3 and 4.4, the effect of the bionic surface on the

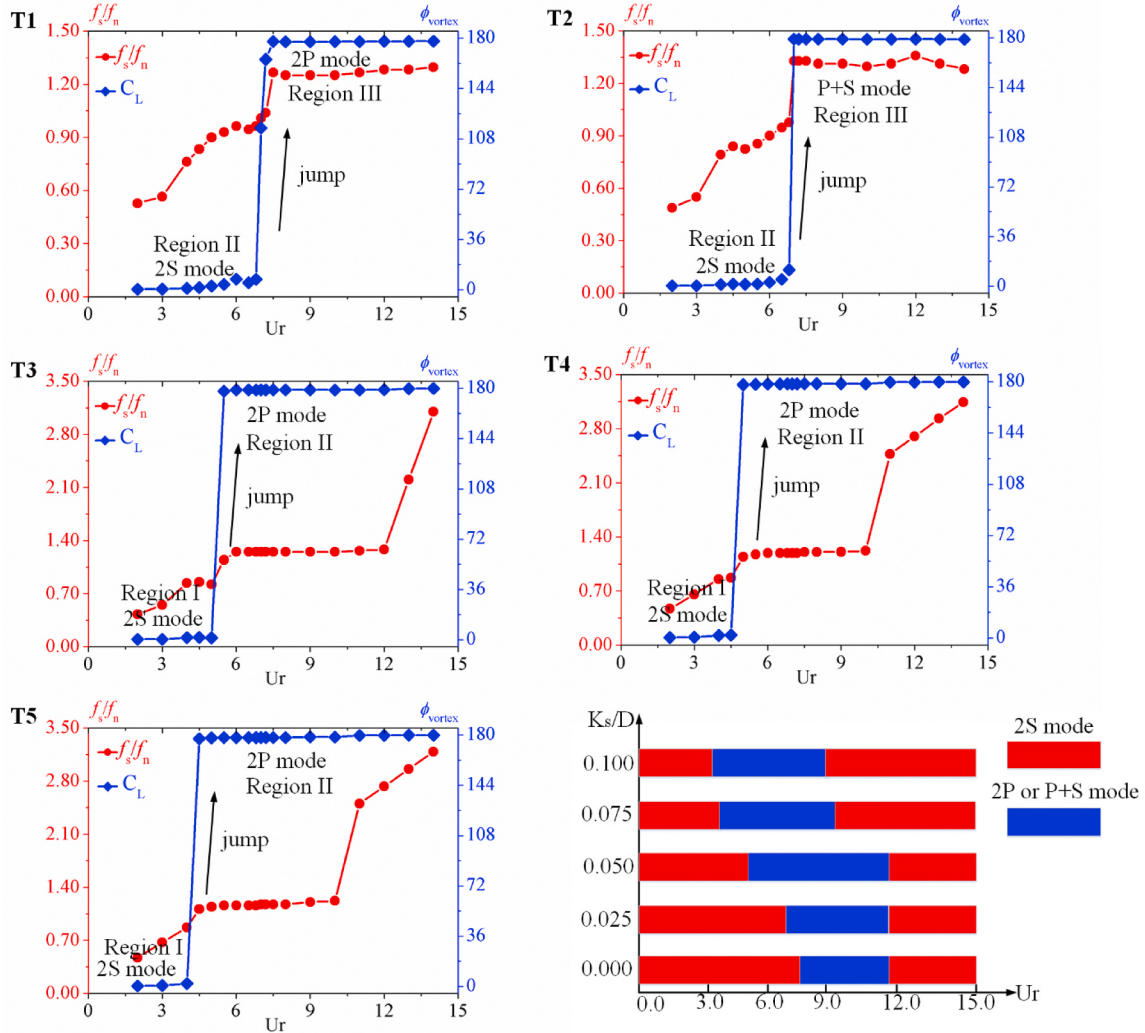


Fig. 16. The vortex phases of five different cylinders.

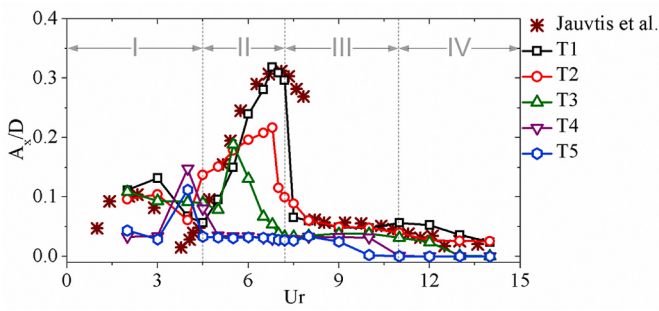


Fig. 17. The in-line amplitude responses of the cylinders with different bionic surfaces.

vortex-induced vibration responses are discussed in detailed. However, the control mechanism of the bionic structure needs to be further understood, so the flow characteristics around the bionic surface are analyzed. Fig. 20 shows the vorticity contours and pressure contours around the bionic surface. Because the boundary layer separation occurs on the cylinder surface, there will be vortex shedding behind the cylinder. Generally, there is a vortex shedding on the upper surface ( $R_1$ ) and a vortex shedding on the lower surface respectively ( $R_2$ ), as shown

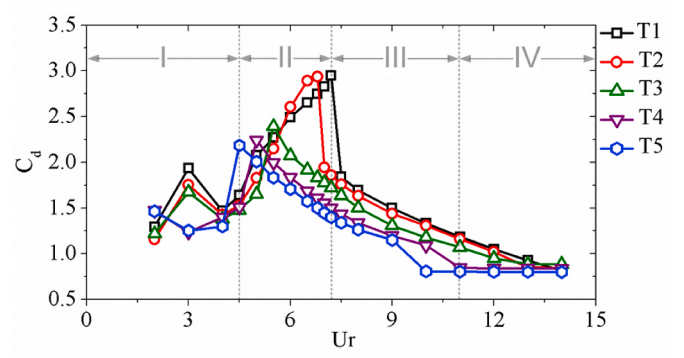
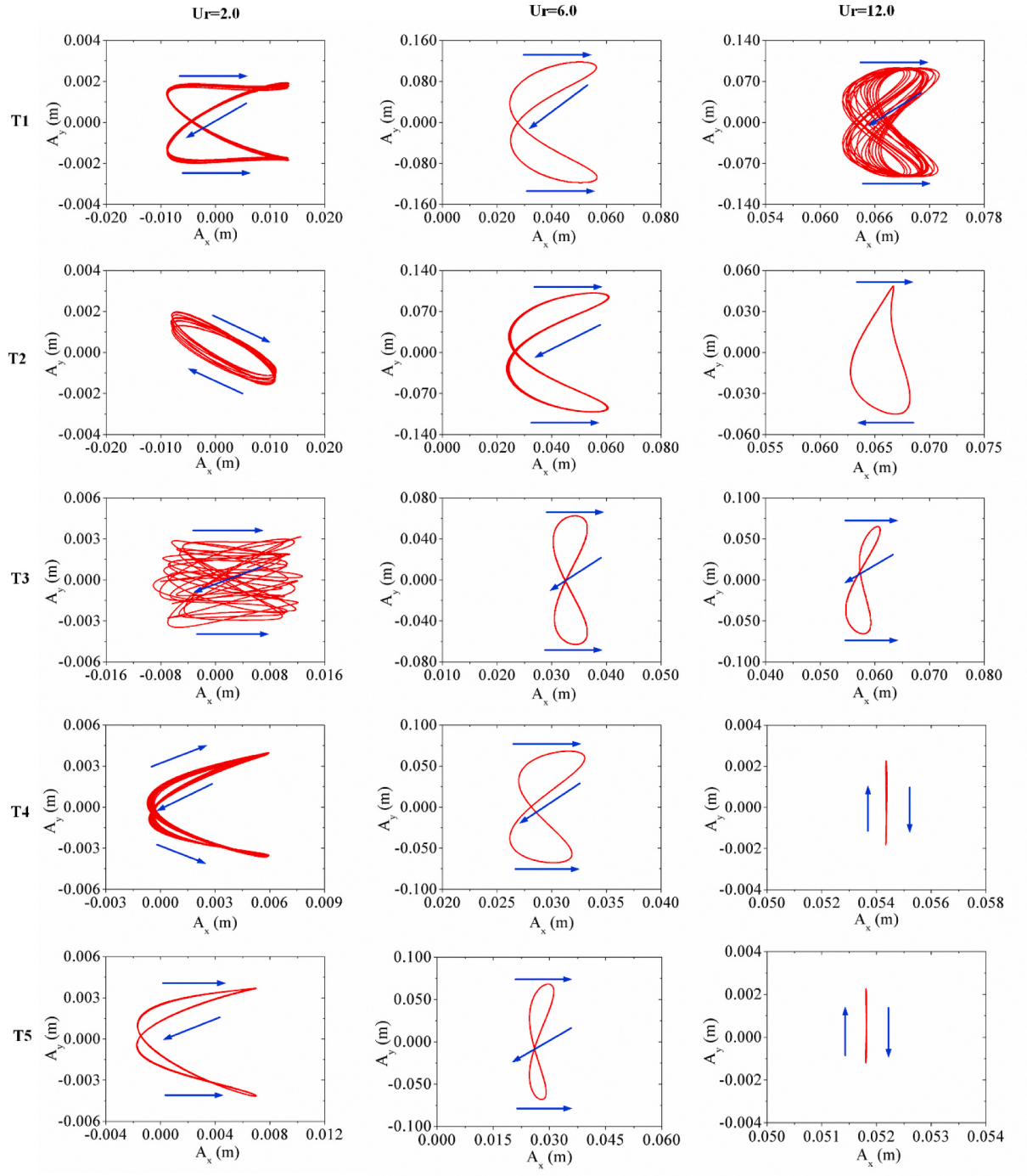


Fig. 18. The mean drag coefficients of the cylinders with different bionic surfaces.

in Fig. 21. And the direction of the vortex is opposite. The distance between the two vortices is  $L$ . Obviously, the interaction between the two vortices is very strong when  $L$  is very small. Both vortices ( $R_1$  and  $R_2$ ) are low-pressure vortices as shown Fig. 20(b), and the strength of the low-pressure vortex is  $V$ . The comparison of distances between the two vortices of T1, T2, T3, T4 and T5 is  $L_5 > L_4 > L_3 > L_2 > L_1$ . The bionic



**Fig. 19.** The motion trajectories of the cylinders with different bionic surfaces.

structure destroys the wake behind the cylinder. Because the coupling strength of two vortices is reduced, the comparison of coupling strength of T1, T2, T3 T4 and T5 is  $V_1 > V_2 > V_3 > V_4 > V_5$ . When  $V$  decreases, the VIV response is suppressed. According to the previous research (Law and Jaiman, 2017), the splitter plate can prevent the interaction of  $R_1$  and  $R_2$ , which is helpful for suppressing VIV responses as shown in Fig. 21(b). Because  $L_5$  is bigger than  $L_1$ , as shown in Fig. 21(a) and (c), the interaction of  $R_1$  and  $R_2$  is suppressed. According to the above analysis, the VIV responses can be suppressed by the bionic structure.

The streamlines around the bionic structure are shown in Fig. 22. Based on Fig. 22(a), the formation area of the boundary layer separation is between P1 and P2. The bionic structure destroys the boundary layer separation between P1 and P2, as shown in Fig. 22 (b) and (c). When the

height of bionic structure is more than a certain value, the boundary layer separation occurs at the sharp point of the ribs. The formation of the smaller vortices is observed between the two sharp points as shown in Fig. 22 (d) and (e). Fig. 22 (f) is the schematic diagram of streamline of T5. As shown in Fig. 22(f), a small vortex is generated between the two sharp points, and the flow will move away from the wall surface after passing the sharp point. Because the smaller vortices can improve the flow characteristics around the cylinder, the area of the low pressure on the cylinder wall is smaller as shown Fig. 20(b).

## 5. Conclusions

Vortex-induced vibration (VIV) of the cylinders with bionic surfaces

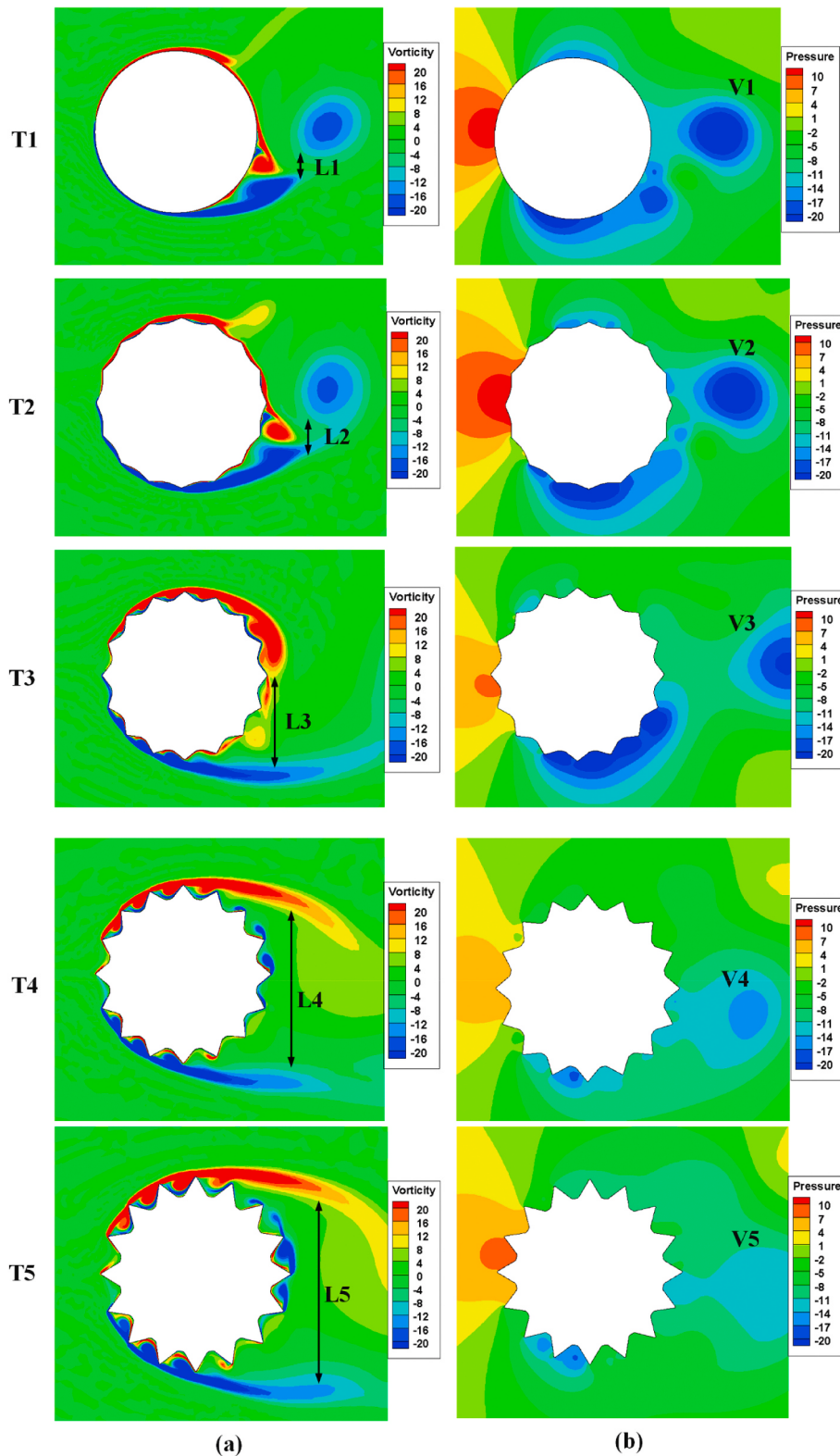


**Fig. 20.** The contours of the cylinder around the bionic surface: (a)vorticity contours and (b) pressure contours ( $Re = 1.2 \times 10^4$ ).

inspired by giant cactus are numerically studied, and the range of Reynolds number is  $8.0 \times 10^3 < Re < 5.6 \times 10^4$ . The computational fluid dynamics (CFD) method is adopted for numerical calculation, and the dynamic response of the structure adopts Newmark-beta method. The effects of different height ratios of the bionic surfaces on VIV suppression are discussed in detail. The following conclusions are justified:

- (1) Based on the VIV responses, the VIV response region is divided into four regions. In region I, the frequency ratios of the different cylinders show a rapid upward trend and the amplitude ratios also show a rapid upward trend. In region II, the frequency ratios of T1, T2, T3, T4 and T5 are close to 1.0, and the lock-in phenomenon gradually occurs in advanced as the height ratio of the

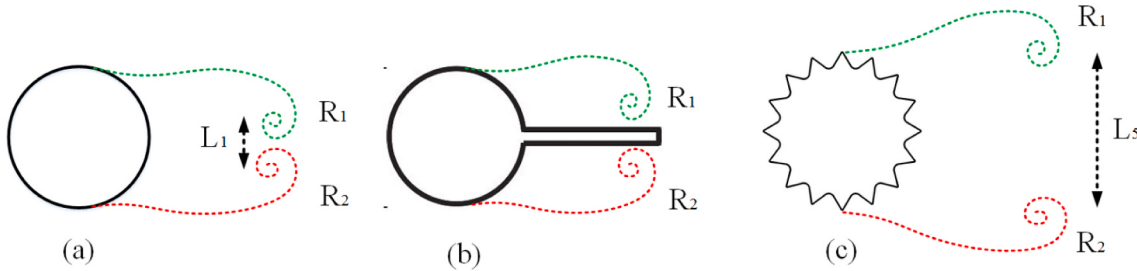


Fig. 21. The schematic diagram of wake vortex shedding.

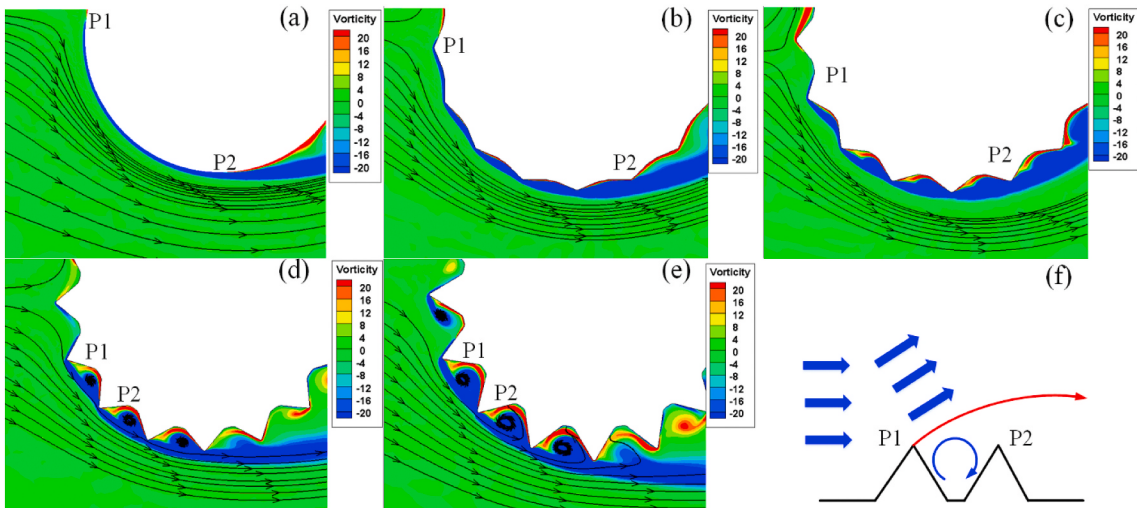


Fig. 22. The streamlines around the bionic structure; (a) T1, (b) T2, (c) T3, (d) T4 and (e) T5. (f) And the schematic diagram of streamline of T5.

bionic surface increases. The amplitude ratios show a rapid upward trend for T1, T2 and T3. The maximum cross-flow amplitude ratio decreases from 1.5 (T1) to 0.75 (T5), which reduces by about 50%. In region III, the frequency ratios of the cylinders are more than 1.0, and they are in a stable lock-in region. For T4 and T5, the amplitude ratios are similar to that in region II, and they do not increase and remains stability. In region IV, the amplitude ratios begin to decrease rapidly. The range of the lock-in region is smaller for T4 and T5 compared with that of T1.

- (2) In region I, the vortex force coefficients, the potential force coefficients of T1, T2, T3, T4 and T5 are in phase, and the total lift force mainly comes from the vortex force. The vortex patterns of T1, T2, T3, T4 and T5 are 2S modes. In region II, the total lift force coefficients and the potential force coefficients of T1 and T2 are out of phase. The phase differences between the potential force coefficients and the vortex force coefficients for T3, T4 and T5 are close to  $\pi$ . The vortex patterns of T1 and T2 are still 2S modes, but the vortex patterns of T3, T4, and T5 are 2P modes. In region III, the phase differences between the potential force coefficients and the vortex force coefficients for T1, T2, T3, T4 and T5 are all about  $\pi$ . With the increase of the height ratio of the bionic surface, the vortex force coefficients and the potential force coefficients decrease gradually. The vortex pattern of T1 is 2P mode, but the vortex patterns of T2, T3, T4 and T5 are P + S modes. The vortex mode is more complex in the lock-in region. In region IV, the total lift force coefficients and the potential force coefficients of T1 and T2 are out of phase.
- (3) For a smooth cylinder (T1), the jump of frequency ratio occurs between region II and region III. When the frequency ratio is more than 1.0, the jump of frequency ratio occurs and the vortex phase jump from about  $0^\circ$  to about  $180^\circ$ . For T2, the jump of

frequency ratio occurs between region II and region III, and the vortex pattern is P + S mode in region III. For T3, T4 and T5, the jump of frequency ratio occurs between region I and region II. The jump of frequency ratio occurs earlier for T3, T4 and T5 compared with that for T1 and T2.

The author provides a method that may be used in engineering practice, and provides some rules that can be used in engineering practice. There are many parameters of the bionic structure that may affect the VIV responses, including the number of ribs ( $N$ ), the height ratio ( $K_s/D$ ) and the shapes of the ribs. In this paper, the parameters of the bionic structure studied are  $N = 16$  and  $0 \leq K_s/D \leq 0.1$ . According to the results of this paper, the parameters of the bionic structure can be optimized, which is helpful to reduce the maximum cross-flow amplitude ratio. This is a very hard work, and it is being researched by authors. The authors hope that the bionic structure can be used in engineering application.

#### CRediT authorship contribution statement

**Wei Wang:** Conceptualization, Methodology, Validation, Formal analysis, Investigation, Writing - original draft, Writing - review & editing, Visualization. **Baowei Song:** Methodology, Resources, Project administration, Funding acquisition. **Zhaoyong Mao:** Methodology, Resources, Project administration, Funding acquisition. **Wenlong Tian:** Software, Methodology, Project administration, Funding acquisition. **Tingying Zhang:** Validation, Data curation.

#### Declaration of competing interest

The authors declare that they have no known competing financial

interests or personal relationships that could have appeared to influence the work reported in this paper.

## Acknowledgement

This research is supported by the National Natural Science Foundation of China (Grant No.10672136, Grant No.61572404 and Grant No.51509205).

## References

- Artana, G., Sosa, R., Moreau, E., Touchard, G., 2003. Control of the near-wake flow around a circular cylinder with electrohydrodynamic actuators. *Exp. Fluid* 35 (6), 580–588.
- Carini, M., Pralits, J.O., Luchini, P., 2014. Feedback control of vortex shedding using a full-order optimal compensator. *J. Fluid Struct.* 53, 15–25.
- Chatterjee D. Dual role of thermal buoyancy in controlling boundary layer separation around bluff obstacles. *Int Commun. Heat Mass.* 56, 152–158.
- Ding, L., Zhang, L., Wu, C.M., Mao, X.R., Jiang, D.Y., 2015. Flow induced motion and energy harvesting of bluff bodies with different cross sections. *Energy Convers. Manag.* 91, 416–426.
- Dorogi, D., Baranyi, L., 2018. Numerical simulation of a freely vibrating circular cylinder with different natural frequencies. *Ocean. Eng.* 158, 196–207.
- Feng, C., 1968. The Measurement of Vortex-Induced Effects in Flow Past a Stationary and Oscillating Circular and D-Section Cylinders. dissertation. University of British Columbia, Vancouver.
- Franzini, G.R., Pesce, C.P., Goncalves, R.T., Fujarra, A.L.C., Mendes, P., 2018. An experimental investigation on concomitant Vortex-Induced Vibration and axial top-motion excitation with a long flexible cylinder in vertical configuration. *Ocean. Eng.* 156, 596–612.
- Gao, Y., Zong, Z., Zou, L., Takagi, S., Jiang, Z.Y., 2018. Numerical simulation of vortex-induced vibration of a circular cylinder with different surface roughnesses. *Mar. Struct.* 57, 165–179.
- Govardhan, R., Williamson, C.H.K., 2000. Modes of vortex formation and frequency response of a freely vibrating cylinder. *J. Fluid Mech.* 420, 85–130.
- Huang, S., 2011. VIV suppression of a two-degree-of-freedom circular cylinder and drag reduction of a fixed circular cylinder by the use of helical grooves. *J. Fluid Struct.* 27 (7), 1124–1133.
- Huera-Huarte, F.J., 2017. Suppression of vortex-induced vibration in low mass-damping circular cylinders using wire meshes. *Mar. Struct.* 55, 200–213.
- Jauvtis, N., Williamson, C.H.K., 2004. The effect of two degrees of freedom on vortex-induced vibration at low mass and damping. *J. Fluid Mech.* 509, 23–62.
- Kang, Z., Cheng, C., Ma, G., 2019. A numerical investigation of the effects of Reynolds number on vortex-induced vibration of the cylinders with different mass ratios and frequency ratios. *Int. J. Nav. Arch. Ocean.* 11 (2), 835–850.
- Khalak, A., Williamson, C.H.K., 1999. Motions, forces and motion transitions in vortex-induced vibration at low mass-damping. *J. Fluid Struct.* 13, 813–851.
- Kiu, K.Y., Stappenberg, B., Thiagarajan, K.P., 2011. Effects of uniform surface roughness on vortex-induced vibration of towed vertical cylinders. *J. Sound Vib.* 330 (20), 4753–4763.
- Law, Y.Z., Jaiman, R.K., 2017. Wake stabilization mechanism of low-drag suppression devices for vortex-induced vibration. *J. Fluid Struct.* 70, 428–449.
- Law, Y.Z., Jaiman, R.K., 2018. Passive control of vortex-induced vibration by spanwise grooves. *J. Fluid Struct.* 83, 1–26.
- Lee, S.J., Lee, J.Y., 2008. PIV measurements of the wake behind a rotationally oscillating circular cylinder. *J. Fluid Struct.* 24 (1), 2–17.
- Muralidharan, K., Muddada, S., Patnaik, B.S.V., 2013. Numerical simulation of vortex induced vibrations and its control by suction and blowing. *Appl. Math. Model.* 37 (1–2), 284–307.
- Pasetto, M., Waisman, H., Chen, J.S., 2019. A waveform relaxation Newmark method for structural dynamics problems. *Comput. Mech.* 63 (6), 1223–1242.
- Rashidi, S., Hayatdavoodi, M., Esfahani, J.A., 2016. Vortex shedding suppression and wake control: a review. *Ocean. Eng.* 126, 57–80.
- Sui, J., Wang, J.S., Liang, S.P., Tian, Q.L., 2016. VIV suppression for a large mass-damping cylinder attached with helical strakes. *J. Fluid Struct.* 62, 125–146.
- Wang, H.K., Zhai, Q., Zhang, J.S., 2018. Numerical study of flow-induced vibration of a flexible plate behind a circular cylinder. *Ocean. Eng.* 163, 419–430.
- Wang, H.B., Ding, L., Zhang, L., Zou, Q.F., Wu, C.M., 2019a. Control of two-degree-of-freedom vortex-induced vibrations of a circular cylinder using a pair of synthetic jets at low Reynolds number: influence of position angle and momentum coefficient. *Int. J. Heat Fluid Flow* 80, 108490.
- Wang, W., Song, B.W., Mao, Z.Y., Tian, W.L., Zhang, T.Y., 2019b. Numerical investigation on VIV suppression of marine riser with triangle groove strips attached on its surface. *Int. J. Nav. Arch. Ocean.* 11 (2), 875–882.
- Wang, W., Mao, Z.Y., Tian, W.L., Zhang, T.Y., 2019c. Numerical investigation on vortex-induced vibration suppression of a circular cylinder with axial-slats. *J. Mar. Sci. Eng.* 7 (12), 454.
- Wang, W., Song, B.W., Mao, Z.Y., Tian, W.L., Zhang, T.Y., Han, P., 2020. Numerical investigation on vortex-induced vibration of bluff bodies with different rear edges. *Ocean. Eng.* 197, 106871.
- Xu, W.H., Ji, C.N., Sun, H., Ding, W.J., Bernitas, M.M., 2019. Flow-induced vibration of two elastically mounted tandem cylinders in cross-flow at subcritical Reynolds numbers. *Ocean. Eng.* 173, 375–387.
- Yamagishi, Y., Oki, M., 2005. Effect of the number of grooves on flow characteristics around a circular cylinder with triangular grooves. *J. Visual-Japan.* 8 (1), 57–64.
- Zdravkovich, M.M., 1981. Review and classification of various aerodynamic and hydrodynamic means for suppressing vortex shedding. *J. Wind Eng. Ind. Aerod.* 7 (2), 145–189.
- Zhu, H.J., Yao, J., 2015. Numerical evaluation of passive control of VIV by small control rods. *Appl. Ocean Res.* 51, 93–116.
- Zhu, H.J., Liao, Z.H., Gao, Y., Zhao, Y., 2017. Numerical evaluation of the suppression effect of a free-to-rotate triangular fairing on the vortex-induced vibration of a circular cylinder. *Appl. Math. Model.* 52, 709–730.